Chapter 5

Cosmic-ray Modulation

5.1 Introduction

This chapter aims to apply the results of the preceding chapters to the study of the modulation of various species of galactic cosmic-rays. To this effect, a three-dimensional, steady state cosmic-ray modulation code, described by *Hattingh and Burger* [1995]; *Burger and Hattingh* [1995]; *Hattingh* [1998] is applied to solve the *Parker* [1965a] cosmic-ray transport equation (TPE)

$$\frac{\partial f_0}{\partial t} = \nabla \cdot \left(\mathbf{K} \cdot \nabla f_0 \right) - \mathbf{V}_{sw} \cdot \nabla f_0 + \frac{1}{3} \left(\nabla \cdot \mathbf{V}_{sw} \right) \frac{\partial f_0}{\partial \ln p}, \tag{5.1}$$

with $f_0(\mathbf{r}, p, t)$ the omnidirectional cosmic-ray distribution function in terms of particle momentum p, related to the cosmic-ray differential intensity by $j_T = p^2 f_0$ [see, *e.g.*, *Gleeson and Axford*, 1967; *Gleeson and Urch*, 1973; *Forman*, 1970; *Webb and Gleeson*, 1979; *Moraal and Potgieter*, 1982; *Moraal*, 2011]. Various processes modulating an initial, interstellar cosmic-ray distribution function are contained within the above equation. These are, in the order in which the terms governing the processes appear on the right hand side of Eq. 5.1, cosmic-ray diffusion and drift due to gradients and curvature of the heliospheric magnetic field, the effects of outward convection of cosmic-rays due to the action of the solar wind, and adiabatic cooling. Possible sources of energetic particles within the heliosphere are neglected.

The above equation can be solved in the steady state by assuming a coordinate system that corotates with the equatorial solar rotation rate Ω, using the relation [*Kóta and Jokipii*, 1983]

$$\frac{\partial f}{\partial t} + \left(\mathbf{\Omega} \times \mathbf{r} \right) \cdot \nabla f = 0, \tag{5.2}$$

to eliminate the explicit time dependence. This procedure reduces the Parker TPE to the form

$$\nabla \cdot \left(\mathbf{K}^S \cdot \nabla \right) - \left(\mathbf{v}_d + \mathbf{V}^* \right) \cdot \nabla f + \frac{1}{3} \left(\nabla \cdot \mathbf{V}^* \right) \frac{\partial f}{\partial \ln p} = 0, \tag{5.3}$$

with $\mathbf{V}^* = \mathbf{V}_{sw} - \mathbf{\Omega} \times \mathbf{r}$. This parabolic equation can be solved by employing the alternating direction implicit (ADI) method [see, *e.g.*, *Peaceman and Rachford*, 1955; *Douglas*, 1962; *Hattingh*, 1998]. For an extensive review of the several previous approaches taken to solve the *Parker*

[1965a] transport equation, as well as in-depth discussions as to the relations between the various quantities pertinent to it, see *Moraal* [2011].

This 3D steady state modulation code, as described by *Hattingh and Burger* [1995]; *Burger and Hattingh* [1995]; *Hattingh* [1998], has the advantage of being able to easily provide information as to such global quantities such as cosmic-ray latitude gradients, as opposed to more recent time-dependent, stochastic TPE solvers such as those used by, *e.g.*, *Zhang* [1999a, b], *Alanko-Huotari et al.* [2007], *Pei et al.* [2010b] and *Strauss et al.* [2011].

Four species of cosmic-rays are considered in this study: protons, electrons, and their respective antiparticles. The proton local interstellar spectrum (LIS) here employed is that used by *Burger et al.* [2008], which is similar to that of *Bieber et al.* [1999] at high energies, but assumes larger values at low energies, such that

$$j_{LIS}^{p^+} = 19.0 \frac{(P/P_0)^{-2.78}}{1 + (P_0/P)^2} \tag{5.4}$$

with units of particles.m^{-2}.s^{-1}.sr^{-1}.MeV^{-1}, and $P_0 = 1$ GV. The electron LIS here used is that of *Langner* [2004], from *Langner et al.* [2001], *viz*.

$$j_{LIS}^{e^-} = \begin{cases} \dfrac{214.32 + 3.32\ln(P/P_0)}{1 + 0.26\ln(P/P_0) + 0.02\left[\ln(P/P_0)\right]^2} \text{ if } P < 0.0026 \text{ GV}, \\ 1.7\left[\dfrac{52.55 + 23.01(P/P_0)}{1 + 148.62(P/P_0)}\right]^2 \text{ if } 0.0026 \text{ GV} \leq P < 0.1 \text{ GV}, \\ \dfrac{1555.89 + 17.36(P/P_0) - 3.4 \times 10^{-3}(P/P_0)^2 + 5.13 \times 10^{-7}(P/P_0)^3}{1 - 11.22(P/P_0) + 7532.93(P/P_0)^2 + 2405.01(P/P_0)^3 + 103.87(P/P_0)^4} \\ \text{if } 0.1 \text{ GV} \leq P \leq 10.0 \text{ GV}, \\ 1.7\exp\left[-0.89 - 3.22\ln(P/P_0)\right] \text{ if } P > 10 \text{ GV}, \end{cases} \tag{5.5}$$

where P_0 is again 1 GV, and with units the same as those of the proton local interstellar spectrum.The antiproton local interstellar spectrum used here is from *Langner and Potgieter* [2004], based on the results of *Moskalenko et al.* [2002] and *Moskalenko et al.* [2003], and given by

$$j_{LIS}^{\bar{p}} = \begin{cases} \exp\left(-9.60 - 0.10\left(\ln E\right)^2 - 1.91\exp(-E)\right) \text{ if } E \leq 0.94 \text{ GeV}, \\ \dfrac{2.42 \times 10^{-3} E^{-2.81}}{\left(0.81 + 7.74E^{-1.81}\right)^2} \text{ if } E > 0.94 \text{ GeV}, \end{cases} \tag{5.6}$$

in terms of kinetic energy E in GeV, with units as for the local interstellar spectra given above. Lastly, the positron local interstellar spectrum used is that of *Della Torre et al.* [2012], based on results presented by *Zhang and Cheng* [2001],

$$j_{LIS}^{e^+} = \frac{45E^{0.7}}{1 + 650E^{2.3} + 1500E^{4.2}}, \tag{5.7}$$

in the same units as the above spectra, with E again in GeV. This local interstellar spectrum, like the local interstellar spectra used by *Potgieter et al.* [2001]; *Langner* [2004], is smaller than observations by, *e.g.*, *Boezio et al.* [2000], at the highest rigidities at Earth. This may be due to a primary positron abundance at higher rigidities due to a source like an astrophysical object

or dark matter annihilation [*Adriani et al.*, 2009b], not included in the LIS. These rigidities, however, are not considered in this study.

The abovementioned cosmic-ray species are studied using the QLT and ENLGC diffusion coefficients as functions of turbulence quantities modelled using the two-component turbulence transport model presented by *Oughton et al.* [2011]. The same turbulence conditions are assumed for each species considered, so as to render as self-consistent a picture of their modulation as possible. It should be noted that throughout what is to follow, a *Parker* [1958] HMF model is assumed as a point of departure, with results acquired by assuming a reduced Schwadron-Parker field as discussed in Subsection 3.3.1 to be considered as a special case. The tilt angle of the heliospheric current sheet was taken to be 5°, the magnetic field magnitude at Earth was chosen to be 5 nT, and the solar wind profile given in Eq. 3.24 was employed, as discussed in Subsection 3.3.1.

The present study assumes a spherical heliosphere with a radius of 100 AU, and does not include the effects of a termination shock or heliosheath. This is a limitation, in that observations and numerical simulations have shown that some modulation can occur within the heliosheath [see, *e.g.*, *Langner*, 2004; *Caballero-Lopez et al.*, 2004b; *Webber*, 2006; *Caballero-Lopez et al.*, 2010; *Burlaga et al.*, 2011], and possibly even beyond that [*Scherer et al.*, 2011]. The exclusion of effects due to the heliosheath is, however, done for two reasons. Firstly, the *Oughton et al.* [2011] was derived assuming an Alfvén speed considerably smaller than the solar wind speed. This is not the case in the heliosheath. Secondly, not much is observationally known for certain as to the large-scale structure and quantities, such as the HMF, solar wind and current sheet profiles, beyond that which has been gleaned from *Voyager* data in the small region traversed by these spacecraft, with even less information available as to the turbulence conditions in this region. Various results of MHD simulations for the large-scale plasma quantities have been published [see, *e.g.*, *Opher et al.*, 2006; *Ferreira et al.*, 2008; *Florinski et al.*, 2011; *Pogorelov et al.*, 2011] but little observational data exists so as to allow for an accurate assessment of the results yielded by these simulations for a large part of the region they describe.

This chapter aims to describe an *ab initio* treatment of the modulation of galactic cosmic rays within the termination shock, with reasonable choices for the transport coefficients, all of which depend on the input of a two-component turbulence transport model. It will be shown that such an approach can in practice lead to results in fair to good agreement with spacecraft observations taken at several locations within the region of interest during solar minimum periods. The *only* free parameter in this approach is the so-called 2D outerscale, and it is therefore the only parameter that may be adjusted to improve fits to cosmic-ray observations. The *modus operandi* here will be to firstly consider proton modulation, and to compare the results yielded by the numerical 3D modulation code, for various choices for the 2D outerscale (see Section 4.7), so as to ascertain the effects and significance of this quantity to proton modulation. These results will be compared to spectra observed at Earth for both magnetic polarity cycles as reported by *McDonald et al.* [1992] (IMP8) and *Shikaze et al.* [2007] (BESS97). Furthermore,

latitude gradients yielded by the modulation code, and calculated using [*Zhang*, 1997; *Burger and Hitge*, 2004; *Burger et al.*, 2008; *Hitge and Burger*, 2010]

$$G_\theta(r) = \frac{1}{\theta_1 - \theta_2} \ln \left[\frac{j_T(r, \theta_2)}{j_T(r, \theta_1)} \right] \times 100\%, \tag{5.8}$$

with $\theta_1 = 90^\circ$ and $\theta_2 = 10^\circ$ colatitude, will be compared with the observations reported by *Heber et al.* [1996] and *de Simone et al.* [2011]. Lastly, to gain a more complete picture of proton modulation, the modulation code results will be compared to the radial intensity profiles reported by *Webber and Lockwood* [2004]. A 'best fit scaling' for the 2D outerscale, based on comparisons with all the datasets mentioned above, will then be proposed, and utilized in all subsequent modulation results. The effects of a reduced Schwadron-Parker field (Subsection 3.3.1) on galactic proton modulation will also be considered, with some focus on the relationship between latitude gradients and relative amplitudes yielded by this modulation approach, for the purposes of comparison with the observed relation between these quantities reported by *Zhang* [1997]. The 'best fit' 2D outerscale model will also be applied to the study of the modulation of antiprotons, with comparisons to the spectra reported at Earth by *Orito et al.* [2000] (BESS95 and BESS97), *Maeno et al.* [2001] (BESS98) and *Adriani et al.* [2010] (PAMELA). Computed antiproton to proton ratios will also be compared with PAMELA results reported by *Adriani et al.* [2009a].

From Sections 4.5 and 4.7, it is clear that the low-rigidity electron mean free paths, both parallel and perpendicular to the HMF, are extremely sensitive to changes in parameters pertaining to the dissipation range of the assumed slab turbulence power spectrum. This sensitivity will be investigated applying the 'best fit' 2D outerscale model discussed in the sections pertaining to proton modulation. Comparisons will be made with solar minimum intensities reported at Earth by *Moses* [1987], *L'Heureux and Meyer* [1976], *Evenson et al.* [1983], *Boezio et al.* [2000] and *Alcaraz et al.* [2000], and with intensities reported at 5 AU by *Potgieter and Ferreira* [1999]. Intensities reported by *Moses* [1987] and *L'Heureux and Meyer* [1976], pertaining as they do to a considerable Jovian component [see also *Ferreira et al.*, 2001a; *Ferreira et al.*, 2001b; *Ferreira*, 2002; *Ferreira et al.*, 2004], are included only for the purposes of comparison as an upper bound for intensities yielded by the 3D modulation code in this study. Conclusions, however, can still be drawn as to the behaviour of low-energy galactic electrons, as the total contribution of this component to the cosmic-ray electron intensity at Earth has been estimated at $\sim 20\%$ [*Ferreira*, 2002]. Computed latitude gradients will be compared to the data point presented by *Heber et al.* [2008].

The dissipation range parameter set providing the most reasonable agreement with electron observations will, along with the 'best fit' 2D outerscale model obtained from the study of proton modulation, be used to compute positron intensities, which will then be compared to spacecraft observations reported by *Boezio et al.* [2000] (CAPRICE94), *Alcaraz et al.* [2000] (AMS), and *DuVernois et al.* [2001] (HEAT). Furthermore, computed positron fractions will be compared with various observations, including those of *Adriani et al.* [2009b].

Note that throughout what is to follow, the turbulence-reduced drift coefficients of *Burger and Visser* [2010], as well as the diffusion coefficients described in the previous chapter, are used in conjunction with the *Oughton et al.* [2011] turbulence transport model, assuming axisymmetric perpendicular diffusion.

5.2 Proton and Antiproton Modulation

5.2.1 Effect of the 2D outerscale on proton modulation

The several simple, *ad hoc* scalings chosen for the 2D outerscale in Section 4.7, and illustrated in Fig. 4.23, are given by

$$\lambda_{out} = k\lambda_{c,2D} \tag{5.9}$$

where $\lambda_{c,2D}$ is the 2D correlation scale, and k is a constant, here chosen to be equal to 10, 100, or 1000; and

$$\lambda_{out} = 100\lambda_{c,2D}(1\ \mathrm{AU}, \theta)\left(\frac{r}{r_e}\right)^{\varrho} \tag{5.10}$$

with ϱ chosen to be 0.2 or 1.0. These scalings are chosen to give an idea of what effect the magnitude and radial dependence of the 2D outerscale would have on cosmic-ray intensities. Furthermore, results for a 'best fit' form for the 2D outerscale, in terms of the computed cosmic-ray intensities, will also be presented. The 2D outerscale is relevant only to the modelled 2D turbulence power spectrum, and hence will not affect the parallel mean free paths used in this study. The proton parallel mean free paths based on the random sweeping model for dynamical turbulence, described and characterized in Sections 4.3 and 4.4 will be used exclusively in this section, as for this particular species the random sweeping and damping turbulence mean free paths are the same, and thus are expected to yield identical results when applied to cosmic-ray modulation. The perpendicular mean free paths corresponding to the various scenarios here considered for the 2D outerscale are characterized in Section 4.7, while the reduced drift scales corresponding to the various forms chosen for λ_{out} are described and characterized in Subsections 4.8.3 and 4.8.5.

Figure 5.1 shows galactic proton differential intensity spectra as functions of kinetic energy at Earth for the cases where λ_{out} is directly proportional to the 2D correlation scale yielded by the *Oughton et al.* [2011] turbulence transport model, with (top panel) and without (bottom panel) the effects of drift. Several sets of spacecraft data taken during solar minimum periods corresponding to positive and negative magnetic polarity cycles are also shown. When drifts are switched off (bottom panel), the smaller 2D outerscales yield the smallest intensities. This is not unexpected, as from Section 4.7 it can be seen that smaller values of the 2D outerscale lead to smaller perpendicular mean free paths. The no-drift spectra for the cases where $\lambda_{out} = 100\lambda_{c,2D}$ and $\lambda_{out} = 1000\lambda_{c,2D}$ are virtually indistinguishable, again due to the very similar perpendicular mean free paths acquired when these forms for the 2D outerscale are used.

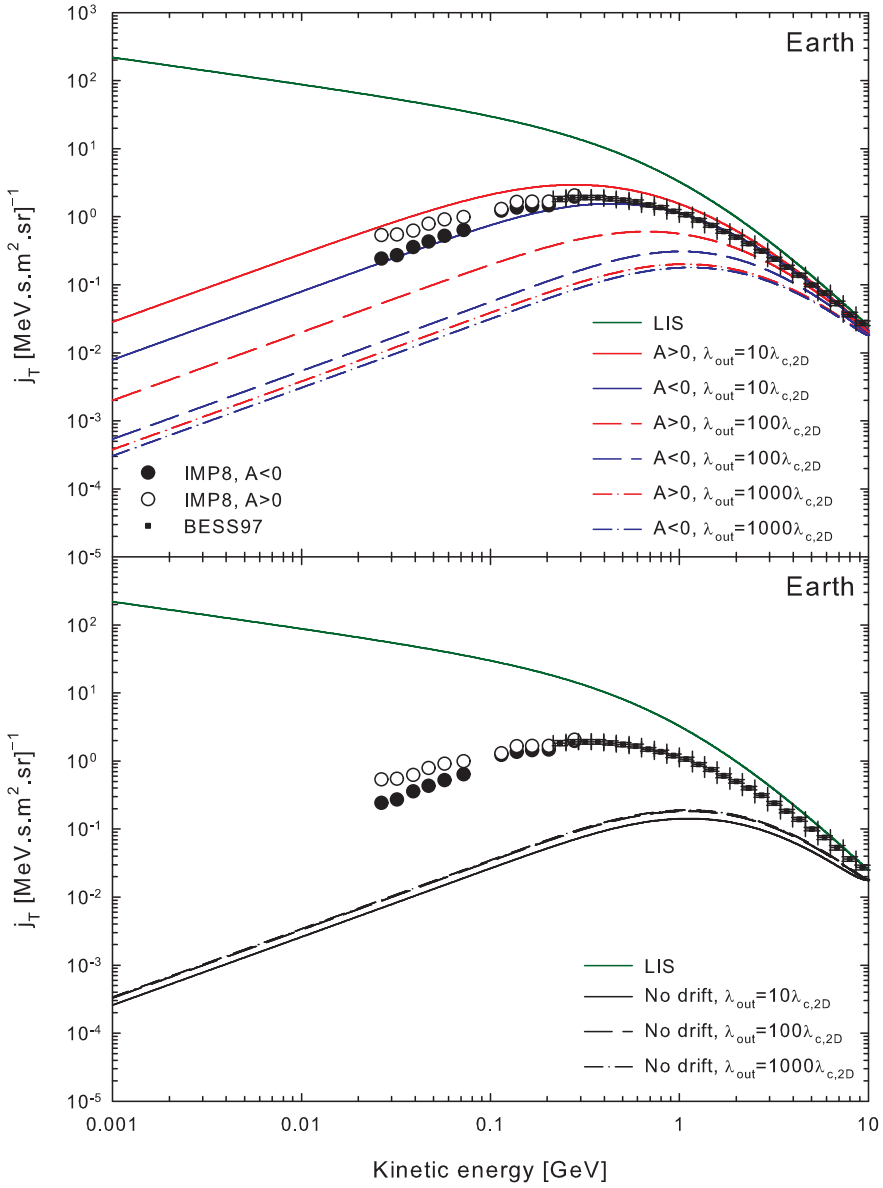

Figure 5.1: Galactic cosmic-ray proton intensity spectra at Earth, as a function of kinetic energy for 2D outerscales that scale as $\lambda_{out} = k\lambda_{c,2D}$. Top panel illustrates cases where drift effects are active, while the bottom panel shows no-drift solutions. Spacecraft data shown are reported by *McDonald et al.* [1992] (IMP8) and *Shikaze et al.* [2007] (BESS97).

This relatively simple scenario is reversed when drift effects are added. Intensities now depend strongly on the levels of drift reduction implicit to the use of a particular form for the 2D outerscale, with larger intensities at 1 AU corresponding to the smallest choice for the 2D outerscale. This can be understood by considering the drift scales characterized in Subsection 4.8.5, where the $\lambda_{out} = 10\lambda_{c,2D}$ scaling yielded drift scales closest to the weak scattering result. It is therefore not surprising that for this case, where drift effects are most significant, the proton intensities are highest, and the separation between solutions corresponding to $A > 0$ and $A < 0$ is the largest. The intensities computed using $\lambda_{out} = 10\lambda_{c,2D}$ come quite close to the data

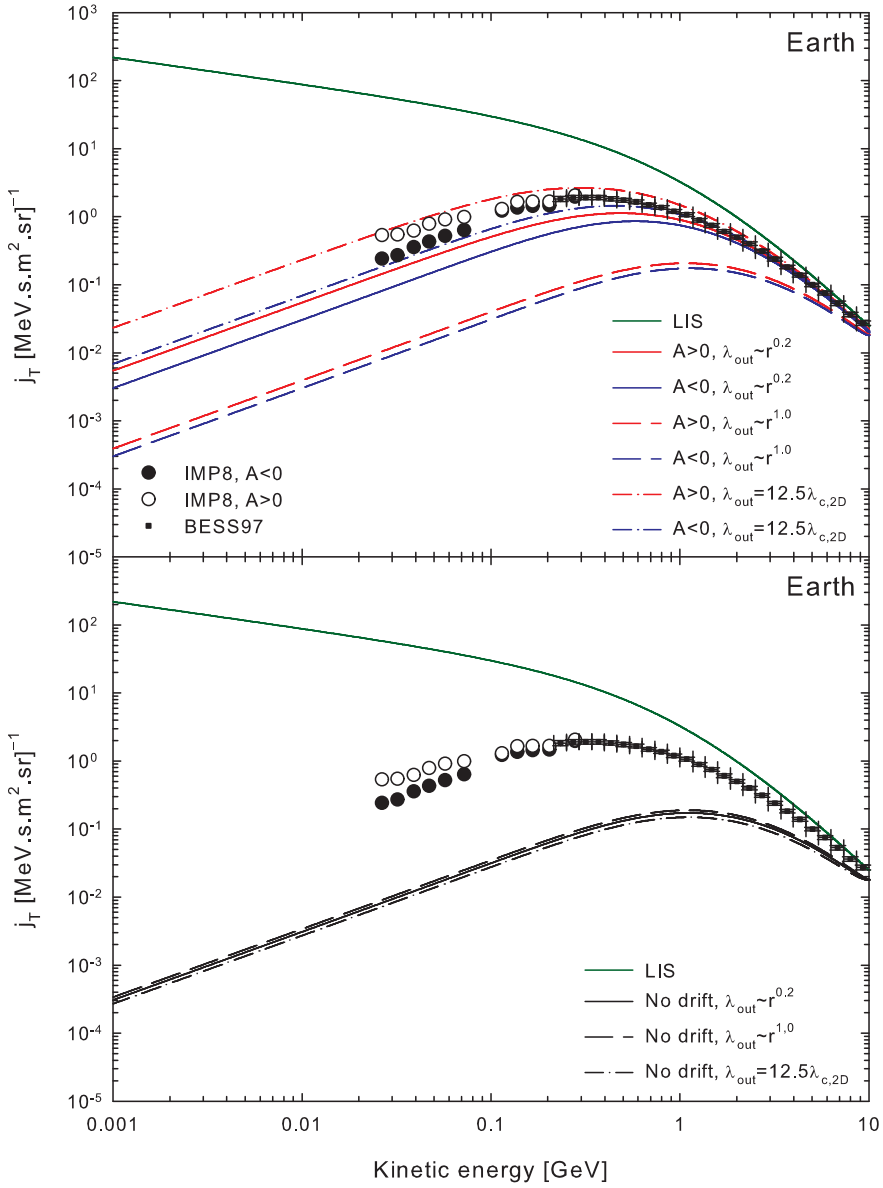

Figure 5.2: Galactic cosmic-ray proton intensity spectra at Earth, as a function of kinetic energy for 2D outerscales that scale as $\lambda_{out} \sim r^{\varrho}$, along with solutions corresponding to $\lambda_{out} = 12.5\lambda_{c,2D}$. Top panel illustrates cases where drift effects are active, while the bottom panel shows no-drift solutions. Spacecraft data shown are reported by *McDonald et al.* [1992] (IMP8) and *Shikaze et al.* [2007] (BESS97).

during $A > 0$, and fall on the IMP8 observations during $A < 0$. Intensities corresponding to $\lambda_{out} = 1000\lambda_{c,2D}$ where drift effects are considered are very close to the no-drift intensities for this form of 2D outerscale, due to the very small drift scales that result from its use. The fact that this choice yields rather unrealistic results can also be interpreted as being encouraging as this scaling yields in some regions of the heliosphere values for the outerscale considerably greater than 100 AU (see the bottom panel of Fig. 4.23, in particular), which may be considered unphysical. The case where $\lambda_{out} = 100\lambda_{c,2D}$ represents an intermediate scenario, yielding intensities bounded by the results of the $\lambda_{out} = 10\lambda_{c,2D}$ and $\lambda_{out} = 1000\lambda_{c,2D}$ scalings.

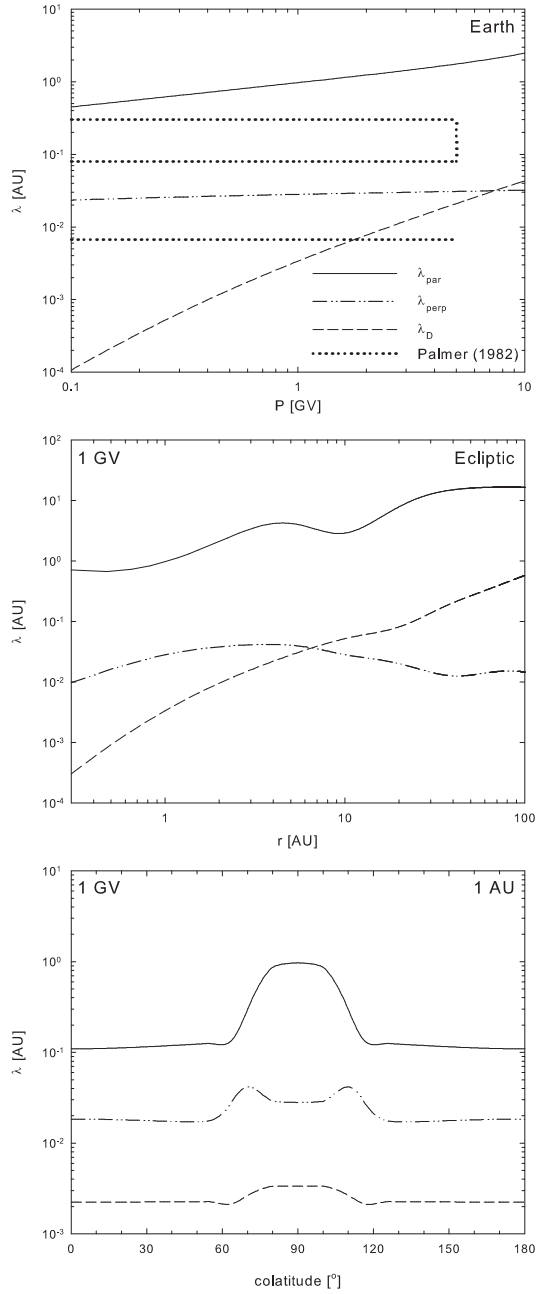

Figure 5.3: Mean free paths and drift scales corresponding to the 'best fit' $\lambda_{out} = 12.5\lambda_{c,2D}$ choice for the 2D outerscale, as a function of rigidity (top panel), heliocentric radial distance in the ecliptic plane (middle panel) and colatitude at 1 AU (bottom panel).

As it turns out, choosing a form for the 2D outerscale such that $\lambda_{out} = 12.5\lambda_{c,2D}$ leads to even better agreement with observations, especially during $A > 0$. Intensities calculated with this outerscale are shown for comparison in Fig. 5.2, where results with $\lambda_{out} \sim r^{\varrho}$ are presented, which is in the same format as Fig. 5.1. From Section 4.7 the perpendicular mean free paths corresponding to choices where $\lambda_{out} \sim r^{\varrho}$ are very similar, with differences appearing only in the outer heliosphere above ~ 2 GV. These differences, however, are not significant enough to lead to very different intensity spectra at Earth when drift effects are omitted (bottom panel).

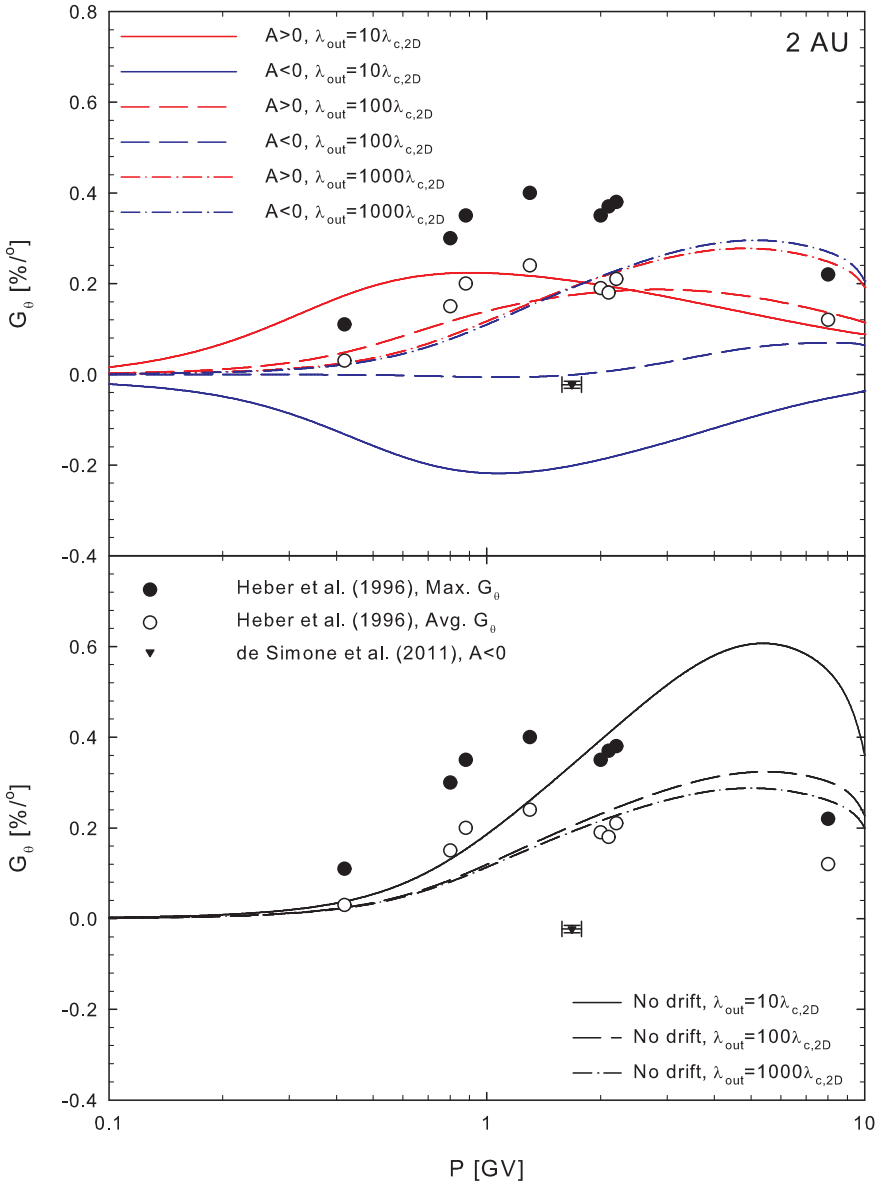

Figure 5.4: Galactic cosmic-ray proton latitude gradients at 2 AU as functions of rigidity for 2D outerscales that scale as $\lambda_{out} = k\lambda_{c,2D}$. Top panel illustrates cases where drift effects are active, while the bottom panel shows no-drift solutions. Spacecraft data shown are reported by *Heber et al.* [1996] (*Ulysses*) and *de Simone et al.* [2011] (*Ulysses*/PAMELA).

This implies that the differences in intensity shown in the top panel of the figure are mostly due to the differences in drift reduction in the outer heliosphere. Drift effects are more reduced for the $\lambda_{out} \sim r^{1.0}$ case in the outer heliosphere, leading to smaller intensities closer in magnitude to the no-drift solution, and a decreased separation between solutions corresponding to $A > 0$ and to $A < 0$. Comparison with the case where $\lambda_{out} = 12.5\lambda_{c,2D}$ clearly shows that it leads to much better fits than the other two, and will be chosen as the 'best fit' outerscale. This case appears to yield results in reasonable agreement with most of the spacecraft data shown. For the sake of completeness, the mean free paths and drift scales corresponding to this 'best fit' 2D outerscale are shown in Fig. 5.3 as functions of rigidity, heliocentric radial distance,

and colatitude. These results are of course very similar to those obtained with $\lambda_{out} = 10\lambda_{c,2D}$ shown in the previous chapter.

Latitude gradients, shown at 2 AU so as to be comparable to data acquired by *Ulysses*, are illustrated as functions of rigidity for scenarios where drift is present (top panel), and absent (bottom panel) in Fig. 5.4 for 2D outerscales proportional to the 2D correlation scale. Note that the current model results should be compared with the average latitude gradients (open circles) calculated by *Heber et al.* [1996]; the maximum values reported by these authors are shown for completeness. When drift effects are absent, the smallest latitude gradients at higher rigidities correspond to the largest values of λ_{out}, which in turn correspond to scenarios with the largest perpendicular mean free paths. Regardless of the form assumed for the 2D outerscale, the *ab initio* approach yields latitude gradients reasonably within the range of observations, even though a Parker HMF model is used, and axisymmetric perpendicular diffusion is assumed. This is the case even for the artificial no-drift scenarios shown, implying that the complex diffusion coefficients used in this study could possibly lead to realistic latitudinal transport of cosmic-rays, at least in the very inner heliosphere.

Latitude gradients for $\lambda_{out} = 10\lambda_{c,2D}$ and $\lambda_{out} = 100\lambda_{c,2D}$ during the $A < 0$ epoch are negative but tend to be somewhat too large in absolute magnitude. The solution corresponding to the form $\lambda_{out} = 100\lambda_{c,2D}$, however, does come close to the single data point shown. The case where $\lambda_{out} = 1000\lambda_{c,2D}$ yields positive latitude gradients for both $A > 0$ and $A < 0$ similar to those when no drifts are considered. This is a consequence of the greatly reduced drift scale resulting from such large values of the 2D outerscale. At the lowest rigidities, $A > 0$ and $A < 0$ solutions corresponding to the largest values for λ_{out} converge sooner, in terms of decreasing rigidity, due to the greater drift reduction for larger values of the 2D outerscale.

The latitude gradients acquired by assuming that $\lambda_{out} \sim r^{0.2}$ and $\lambda_{out} \sim r^{1.0}$ are shown in Fig. 5.5, in the same format as the previous figure, along with those corresponding to a choice of $\lambda_{out} = 12.5\lambda_{c,2D}$. When drifts are ignored, latitude gradients at higher rigidities corresponding to a choice of $\lambda_{out} \sim r^{1.0}$ are smaller than those yielded by the $\lambda_{out} \sim r^{0.2}$ case, due to the differences in the perpendicular mean free paths at large radial distances yielded by these choices of 2D outerscale. These differences, however, disappear below ~ 1 GV, due to the fact that in the inner heliosphere the perpendicular mean free paths acquired using these forms for λ_{out} are essentially identical. When drift effects are considered, the $A > 0$ latitude gradients for $\lambda_{out} \sim r^{0.2}$ are in relatively good agreement with the observations reported by *Heber et al.* [1996] and somewhat smaller than those for the 'best fit' case. For $A < 0$ the latitude gradients are similarly smaller in magnitude than for the 'best fit' case, and therefore a little closer to the single data point. The latitude gradients computed for both $A < 0$ and $A > 0$ when $\lambda_{out} \sim r^{1.0}$ resemble the latitude gradients for the no-drift scenario, due to the smaller drift scales resulting from this choice of 2D outerscale. Computed $A > 0$ latitude gradients for the 'best fit' case where $\lambda_{out} = 12.5\lambda_{c,2D}$ agree reasonably well with the observations shown at high rigidities, but less so at low rigidities, with poorer agreement between the $A < 0$ latitude

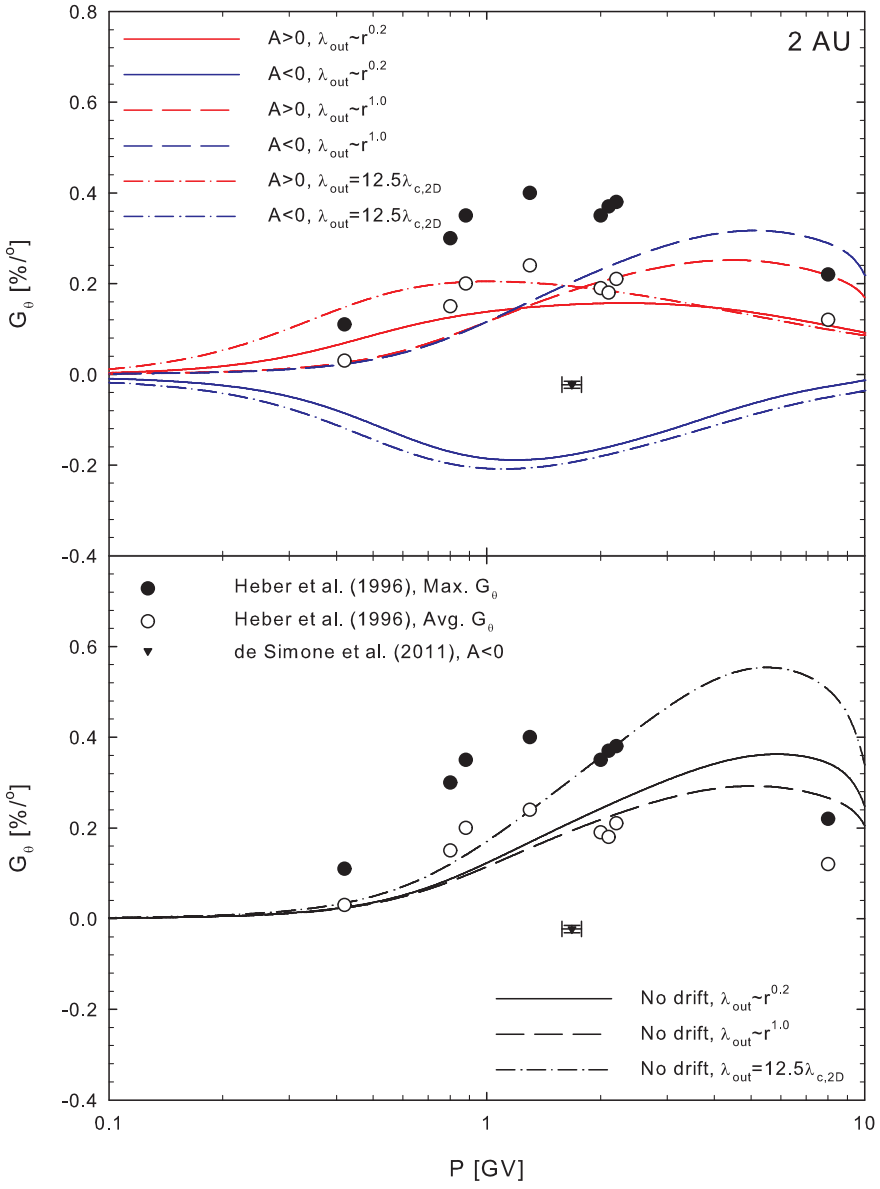

Figure 5.5: Galactic cosmic-ray proton latitude gradients at 2 AU as a function of rigidity for 2D outerscales $\lambda_{out} \sim r^{\varrho}$, along with solutions corresponding to $\lambda_{out} = 12.5\lambda_{c,2D}$. Top panel illustrates cases where drift effects are active, while the bottom panel shows no-drift solutions. Spacecraft data shown are reported by *Heber et al.* [1996] (*Ulysses*) and *de Simone et al.* [2011] (*Ulysses*/PAMELA).

gradients and the *de Simone et al.* [2011] data point.

Figures 5.6 and 5.7 show 0.75 GeV and 0.175 GeV galactic proton intensities as functions of radial distance for the several forms here considered for the 2D outerscale. The *Webber and Lockwood* [2004] data shown are from several spacecraft, some of which (*e.g.* the *Voyagers*) having trajectories that lead them far off the solar ecliptic plane. Therefore, to facilitate comparisons with these data, intensities yielded by the modulation code for the applicable energies are taken at positions in the model heliosphere corresponding to the location of the relevant spacecraft along its particular trajectory. For the cases in Fig. 5.6 where λ_{out} is taken to be directly

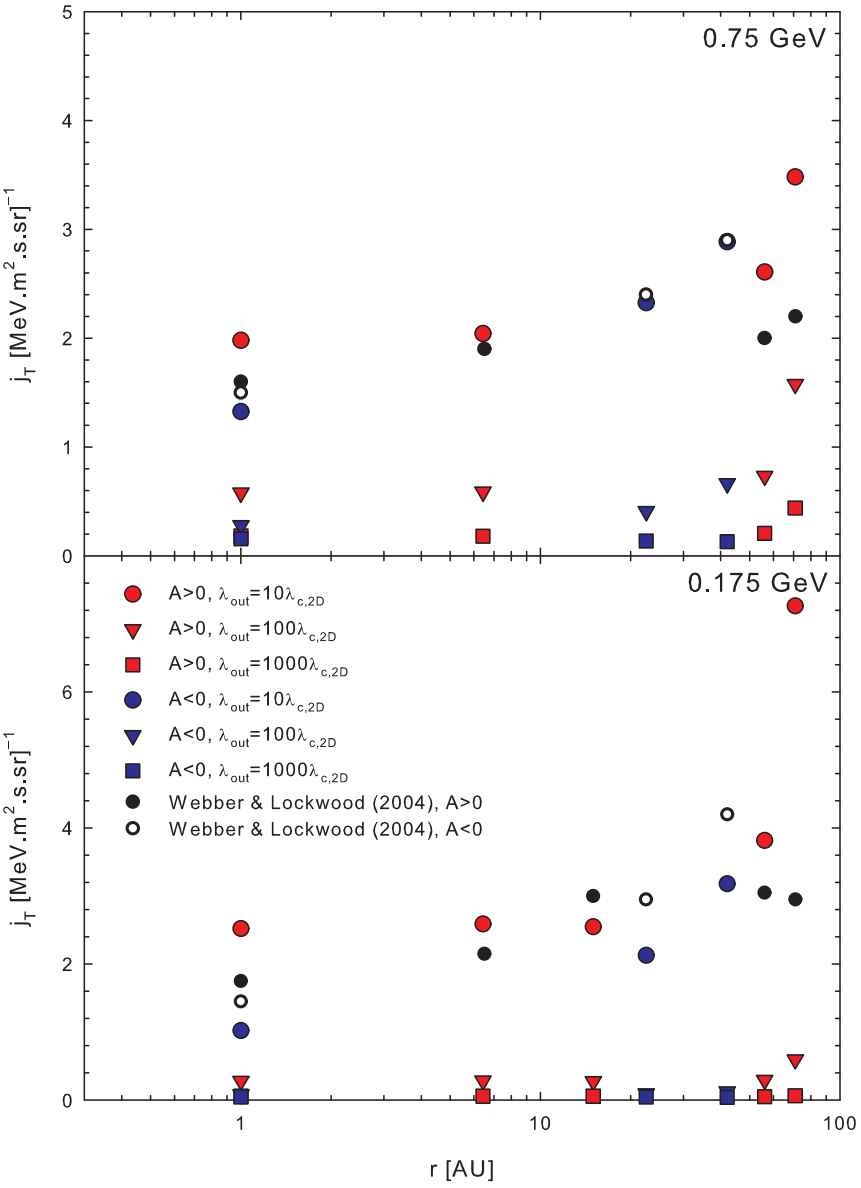

Figure 5.6: Galactic cosmic-ray proton intensities as a function of heliocentric radial distance for 2D outerscales that scale as $\lambda_{out} = k\lambda_{c,2D}$. Top panel illustrates intensities at 0.75 GeV, while the bottom panel shows intensities at 0.175 GeV. Spacecraft data shown are reported by *Webber and Lockwood* [2004] (IMP8, *Pioneer 10*, *Voyager 1* and *Voyager 2*). Modulation code intensities are taken at the applicable spacecraft position.

proportional to the 2D correlation length, the same general trend as that seen for the 1 AU intensity spectra can be observed: larger values for the 2D outerscale lead to smaller differential intensities, during both magnetic polarity cycles, and for both energies shown. Intensities for the case where $\lambda_{out} = 10\lambda_{c,2D}$ are quite close to the data points in the inner heliosphere for both $A > 0$ and $A < 0$, but this reasonable agreement becomes less good at larger radial distances, with computed intensities considerably larger than observations. Cosmic-rays detected by the spacecraft in the outer heliosphere may have experienced more modulation, due to the conditions prevalent in the heliosheath, than is accounted for in this model. This behaviour can

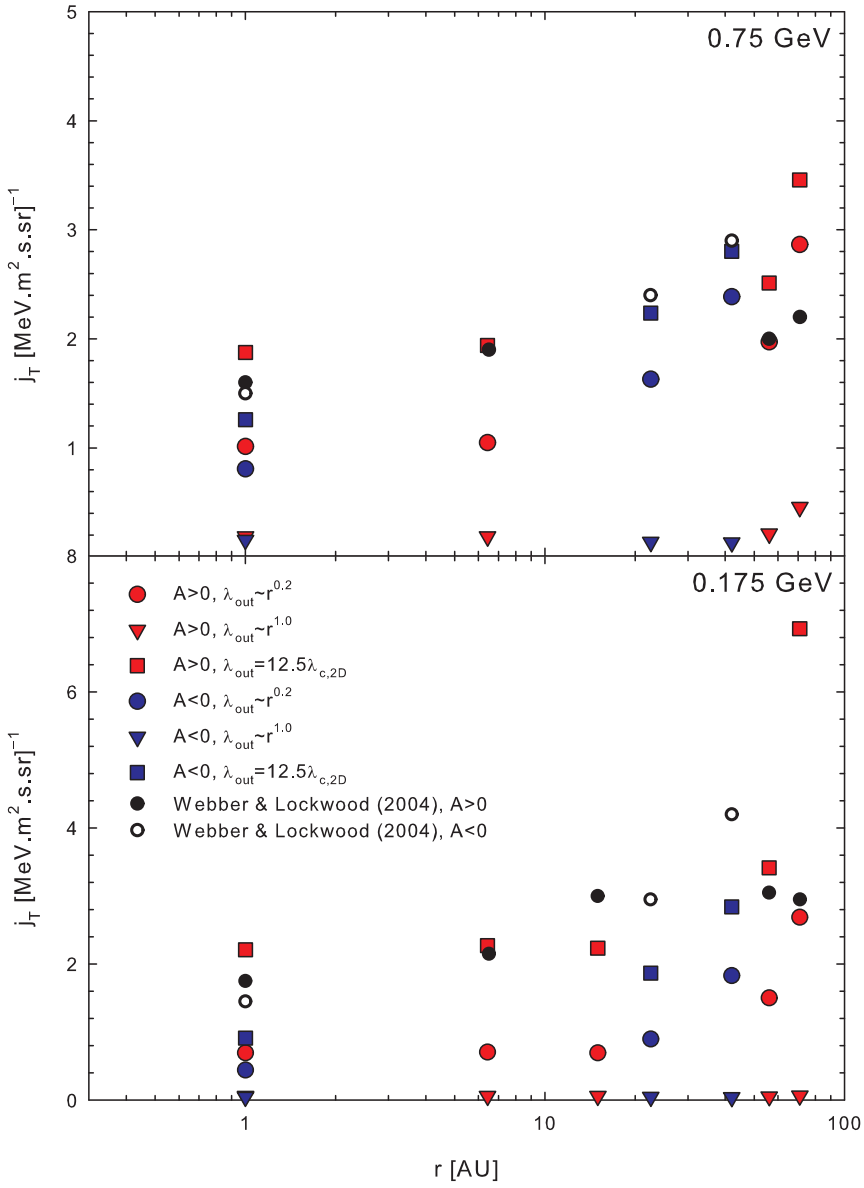

Figure 5.7: Galactic cosmic-ray proton intensities as a function of heliocentric radial distance for 2D outerscales that scale as $\lambda_{out} \sim r^{\varrho}$, along with solutions corresponding to $\lambda_{out} = 12.5\lambda_{c,2D}$. Top panel illustrates intensities at 0.75 GeV, while the bottom panel shows intensities at 0.175 GeV. Spacecraft data shown are reported by *Webber and Lockwood* [2004] (IMP8, *Pioneer 10*, *Voyager 1* and *Voyager 2*). Modulation code intensities are taken at the applicable spacecraft position.

also be seen in Fig. 5.7 for the case where $\lambda_{out} = 12.5\lambda_{c,2D}$, which leads to computed intensities during $A > 0$ in somewhat better agreement with observations in the inner heliosphere. For the case where $\lambda_{out} \sim r^{1.0}$, intensities are very low, and reflect the reduced drift effects resulting from the large values assumed by the 2D outerscale in the outer heliosphere due to the steeper radial dependence chosen for this quantity. The flatter radial dependence chosen when $\lambda_{out} \sim r^{0.2}$ leads to smaller outerscales in the outer heliosphere, which implies less drift reduction in this region and better agreement with observations.

Given the sensitivity of modelled proton intensities and latitude gradients to the choice of 2D outerscale demonstrated here, for further investigation as to the effects of other parameters, and the modulation of other cosmic-ray species, the $\lambda_{out} = 12.5\lambda_{c,2D}$ scaling will be used henceforth as a reference form for this quantity. This choice is motivated simply by the fact that this form for the 2D outerscale yields, relatively speaking, the best consensus agreement with the multiple sets of cosmic-ray spacecraft data considered, for both $A > 0$ and $A < 0$. The disparity between the computed intensities at the greatest radial distances considered in Fig. 5.7 and the corresponding *Webber and Lockwood* [2004] observations is not necessarily a disqualifier in terms of the selection of a 'best fit' scaling for this quantity, as such a result would be expected, given the observed modulation in the heliosheath [see, *e.g.*, *Webber*, 2006; *Burlaga et al.*, 2011], an effect not considered in this study.

5.2.2 Effects of a reduced Schwadron-Parker hybrid HMF

Given the results presented earlier on the reduction of latitude gradients in the presence of an unmodified Parker field, the question naturally arises as to what effect a Fisk-type field would have on proton modulation in this *ab initio* framework. As discussed and motivated in Subsection 3.3.1, the effects of a Schwadron-Parker hybrid field as constructed by *Hitge and Burger* [2010] will be considered here, but reduced in effect as proposed and motivated by *Sternal et al.* [2011]. These effects will then be compared with results acquired using only a pure Parker HMF. The 2D outerscale for both cases considered here is the same, $\lambda_{out} = 12.5\lambda_{c,2D}$. For both fields the boundary values for the *Oughton et al.* [2011] turbulence transport model will be held the same, as in Subsection 3.3.3. As demonstrated in Subsection 3.4.1, the reduced Schwadron-Parker field has a very small effect on the turbulence quantities yielded by the *Oughton et al.* [2011] model.

Considering differential intensity spectra at Earth, shown as functions of kinetic energy in Fig. 5.8 for both HMF models in the presence and absence of drifts, the effects of using the reduced Schwadron-Parker field, as opposed to those of using a purely Parker field, are negligible. In the absence of drift effects, use of this hybrid field leads to somewhat larger intensities due to the marginally increased latitudinal transport that is a result of the latitudinal excursions of the Schwadron-Parker field lines. Figure 5.9, showing latitude gradients for both fields in scenarios with and without the effects of drift, also demonstrates a relatively modest effect when the reduced Schwadron-Parker hybrid field is employed. For all cases shown, the Schwadron-Parker field acts so as to reduce latitude gradients in absolute magnitude, due again to its structure allowing for an enhanced role for the parallel diffusion coefficient in the latitudinal transport of galactic protons.

Fisk-type fields have also provided an elegant explanation for the persistence of recurrent cosmic-ray variations up to the highest latitudes. Variations with a periodicity of ~ 26 days have been observed by *Ulysses* at all latitudes covered by this spacecraft [*Simpson et al.*, 1995a, b; *Heber and Burger*, 1999]. Various mechanisms have been proposed to explain this phenomenon.

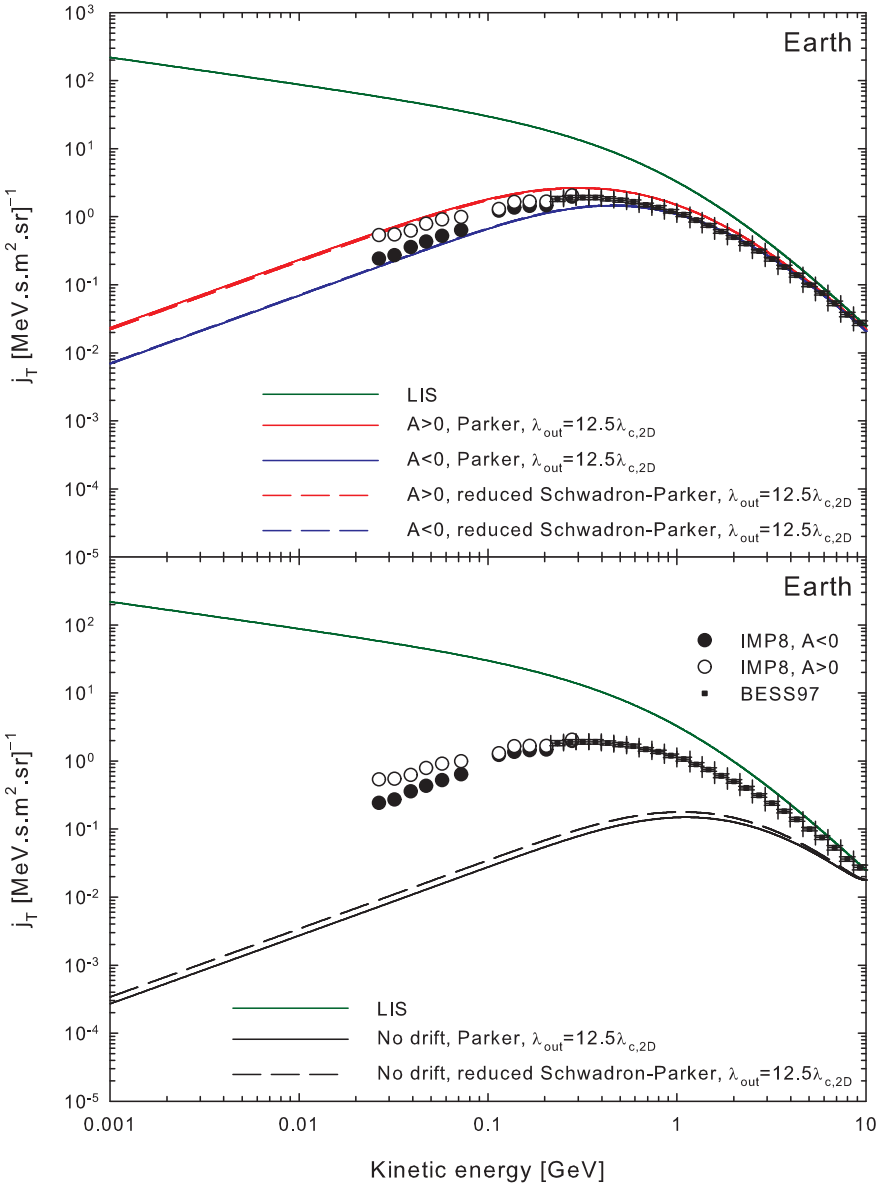

Figure 5.8: Galactic cosmic-ray proton intensity spectra at Earth as a function of kinetic energy for 2D outerscales that scale as $\lambda_{out} = 12.5\lambda_{c,2D}$, for both the Parker (solid lines) and reduced Schwadron-Parker (dashed lines) heliospheric magnetic field models. Top panel illustrates cases where drift effects are active, while the bottom panel shows no-drift solutions. Spacecraft data shown are reported by *McDonald et al.* [1992] (IMP8) and *Shikaze et al.* [2007] (BESS97).

Kóta and Jokipii [1995a, 1998] proposed that the action of corotating interaction regions (CIRs) may be responsible, but as these persist only to intermediate latitudes [*Gosling and Pizzo*, 1999], the high latitude variations cannot easily be explained by CIRs. *Zhang* [1997] also discounts any possible wavy current sheet effects as being responsible for the high-latitude 26-day variations. Enhanced perpendicular diffusion has been invoked [*Jokipii et al.*, 1995; *Giacalone*, 1999b] as a possible mechanism to allow for the effects of corotating interaction regions to be observed at the highest latitudes. Another possible means to this end lies in the action of a *Fisk* [1996]-type heliospheric magnetic field, where different latitudes could be directly connected

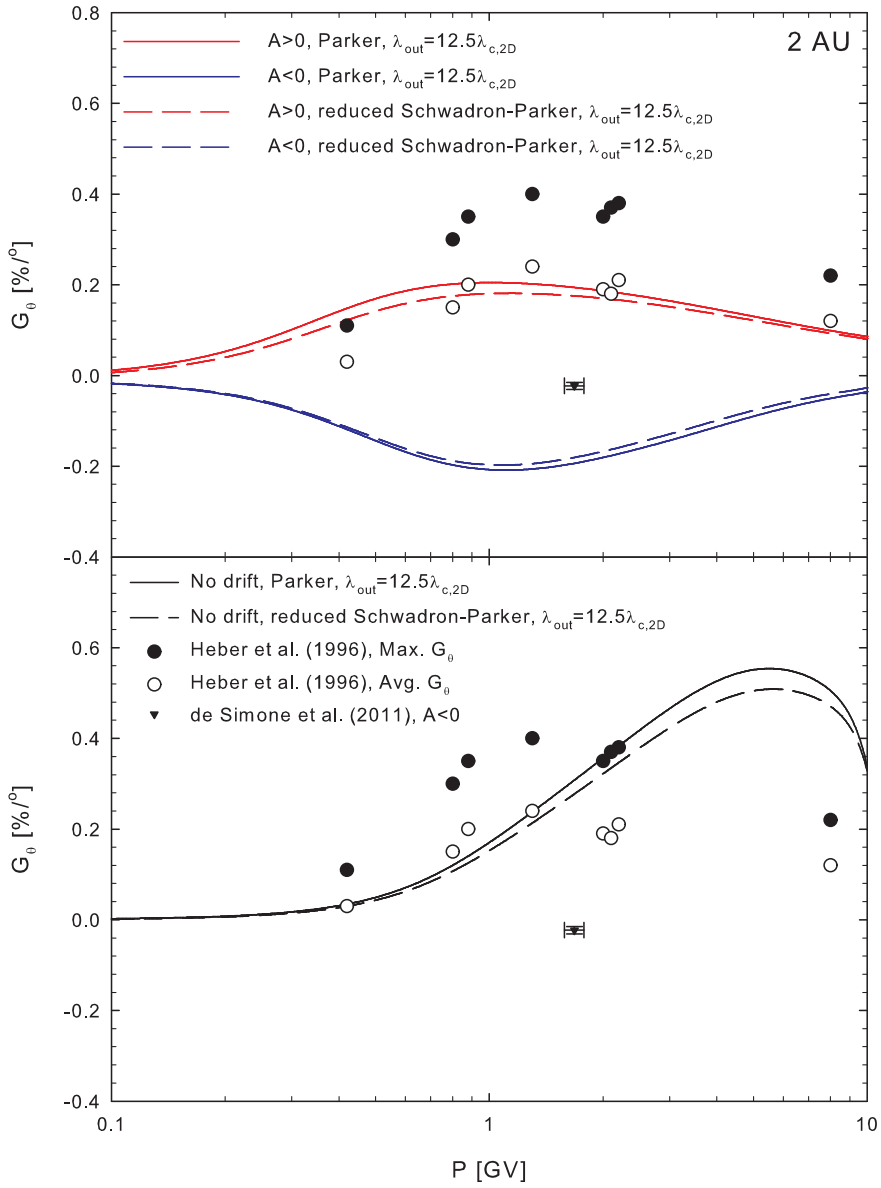

Figure 5.9: Galactic cosmic-ray proton latitude gradients at 2 AU as a function of rigidity for 2D outer-scales $\lambda_{out} = 12.5\lambda_{c,2D}$, for both the Parker (solid lines) and reduced Schwadron-Parker (dashed lines) heliospheric magnetic field models. Top panel illustrates cases where drift effects are active, while the bottom panel shows no-drift solutions. Spacecraft data shown are reported by *Heber et al.* [1996] (*Ulysses*) and *de Simone et al.* [2011] (*Ulysses*/PAMELA).

by magnetic field lines (see *Fisk and Jokipii* [1999]).

Zhang [1997] reports a linear relationship between relative amplitudes and latitude gradients calculated from *Ulysses* data that is independent of particle species or energy. Furthermore, *Richardson et al.* [1999] find that the magnitude of these variations are larger during periods of positive polarity than during the $A < 0$ epoch, implying that the slope of the linearity between latitude gradients and relative amplitudes will be smaller during $A < 0$ than during $A > 0$. *Zhang* [1997], as well as *Paizis et al.* [1997] and *Paizis et al.* [1999], argue that a corre-

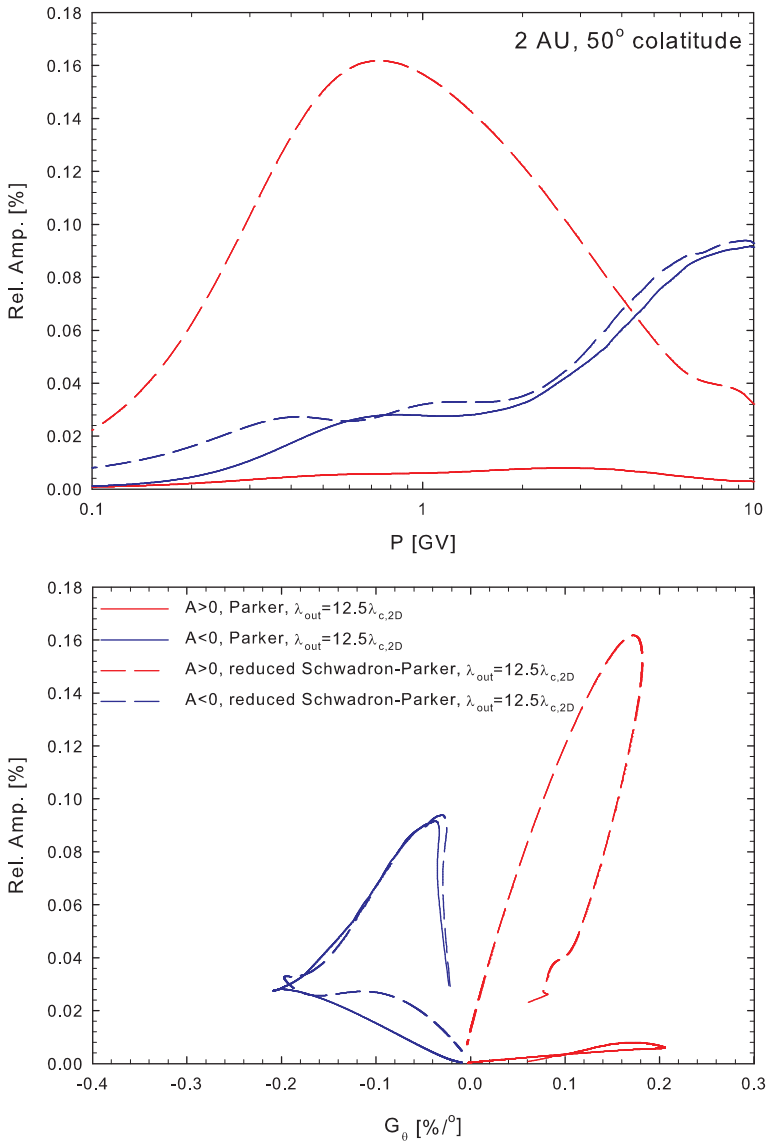

Figure 5.10: Galactic cosmic-ray proton relative amplitudes at 2 AU and $50°$ colatitude, as a function of rigidity (top panel) and corresponding latitude gradient (bottom panel) for a 2D outerscales where $\lambda_{out} = 12.5\lambda_{c,2D}$, for both the Parker and reduced Schwadron-Parker heliospheric magnetic field models. Note that the inner parts of the curves, originating at $(0, 0)$, are for the lowest rigidities.

lation between the 'local' relative amplitudes and 'global' latitude gradients can be due to a particular heliospheric magnetic field configuration if this field were global in effect, and displayed some form of recurrent variations. Furthermore, these authors argue on the basis of the one-dimensional force-field approximation (see *Gleeson and Axford* [1968]), that similar rigidity dependences for both the latitude gradients and relative amplitudes could be explained by similar rigidity dependences of the effective diffusion coefficients governing these phenomena, leading to a linear relationship between these quantities. *Burger et al.* [2008], *Engelbrecht and Burger* [2010], *Hitge and Burger* [2010] and *Sternal et al.* [2011] showed that this linear relationship between the latitude gradients and relative amplitudes can indeed be reproduced by

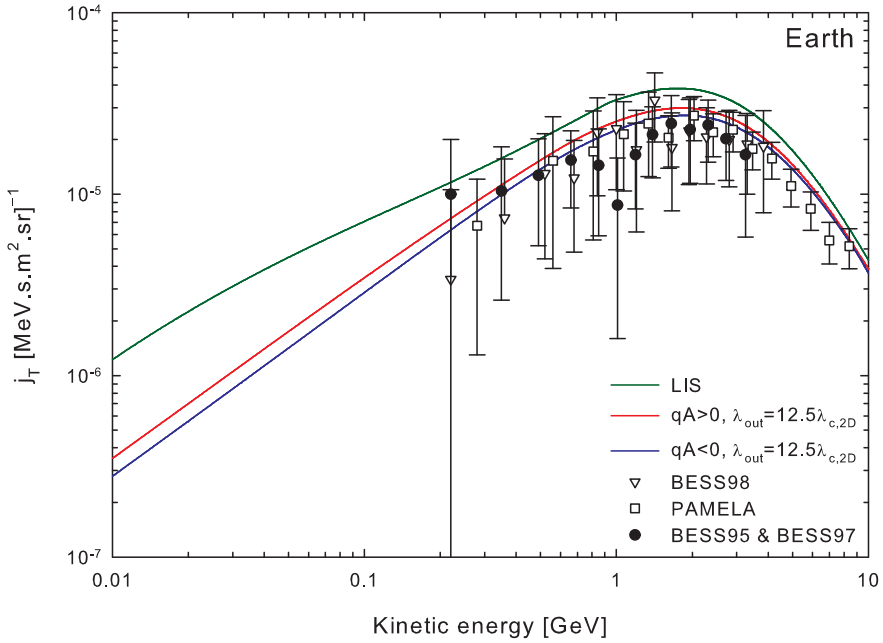

Figure 5.11: Galactic cosmic-ray antiproton intensity spectra at Earth as a function of kinetic energy for a 2D outerscale that scales as $\lambda_{out} = 12.5\lambda_{c,2D}$. Spacecraft data shown are reported by *Orito et al.* [2000] (BESS95 and BESS97), *Maeno et al.* [2001] (BESS98) and *Adriani et al.* [2010] (PAMELA).

means of simulations incorporating various incarnations of Fisk-type fields, implying that the effective diffusion coefficients pertinent to these quantities could indeed be similar, and governed to some degree by the geometry implicit to these HMF models. These numerical studies, however, employed relatively *ad hoc* scalings for the various applicable turbulence quantities, and the effect of the more *ab initio* approach to these quantities taken here on the behaviour of the relative amplitudes, and by extension their relationship to the latitude gradients, would be of some interest.

Figure 5.10 illustrates both the relative amplitudes yielded by the 3D modulation code as functions of rigidity (top panel), and of the latitude gradients (bottom panel), for both a Parker and a reduced Schwadron-Parker HMF. A cursory viewing of the top panel of this figure reveals that the reduced Schwadron-Parker field does yield relative amplitudes that are larger than those acquired assuming a Parker field for both magnetic polarities. However, the qualitatively similar results for $A < 0$, and especially the quantitative agreement in the 'inverted V' part of the loop, suggest that for both field configurations it is the interaction of drifting particles with the wavy neutral sheet that causes these recurrent variations. Nevertheless, when this "inverted V" part of the curves is neglected, the amplitudes for the Schwadron-Parker HMF are larger for $A > 0$ than for $A < 0$, and this is as least in qualitative agreement with the findings of *Richardson et al.* [1999]. The magnitude of these relative amplitudes, however, is clearly very low compared with the findings of *Zhang* [1997], who reports values of between $0.8 \pm 1.0\%$ and $6.5 \pm 2.0\%$. An enhanced Fisk-effect may alter this situation, but can unfortunately not be considered in the present study, due to issues with stability with the 3D code

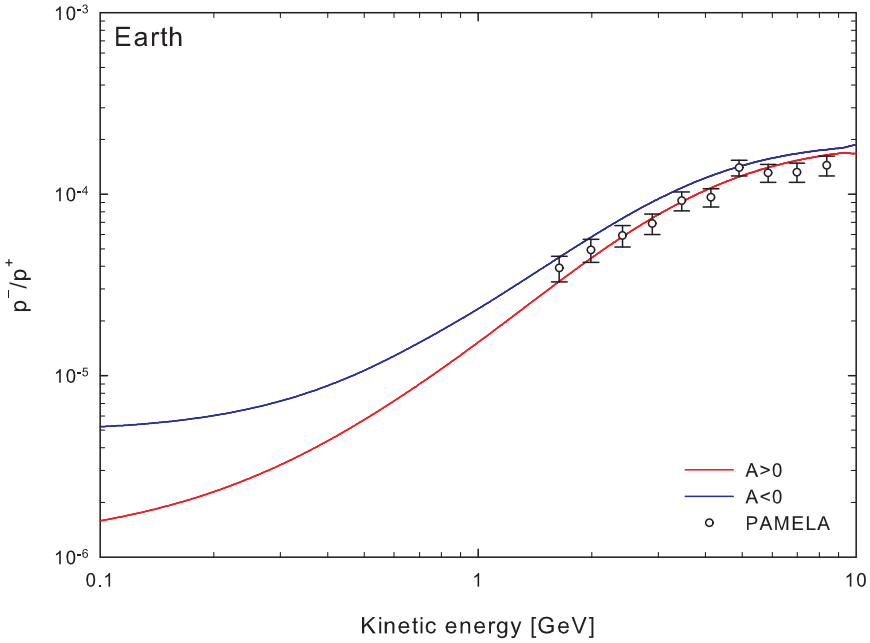

Figure 5.12: Computed galactic cosmic-ray antiproton to proton ratios at Earth, as a function of kinetic energy for a 2D outerscale that scales as $\lambda_{out} = 12.5\lambda_{c,2D}$. Pamela observations shown are reported by *Adriani et al.* [2009a].

that arise when a full Schwadron-Parker hybrid field as proposed by *Hitge and Burger* [2010] is implemented.

5.2.3 Antiprotons

In the framework presented here, the diffusion coefficients for antiprotons are expected to be the same as those for protons, but due to their opposite charge, antiprotons are expected to drift in the opposite direction to protons. Therefore the aim here is to ascertain whether the treatment outlined above for protons would yield results in agreement with observations without any other changes made.

The mean free paths for antiprotons are held to be the same as for protons, and thus follow from the random sweeping QLT result described in Sections 4.3 and 4.4, and the ENLGC perpendicular mean free path described in Sections 4.6 and 4.7. Drift coefficients are again treated as described in Subsections 4.8.3 and 4.8.5. The 2D outerscale is chosen such that $\lambda_{out} = 12.5\lambda_{c,2D}$, and a purely Parker HMF is assumed. The local interstellar spectrum used is that employed by *Langner and Potgieter* [2004], based on results presented by *Moskalenko et al.* [2002, 2003], and expressed by Eq. 5.6. Given the level of observations of antiproton intensities at Earth, this local interstellar spectrum may be too low [*Moskalenko et al.*, 2002]. This may not be a serious issue, since the uncertainties in antiproton intensities observed at Earth are quite high [see, *e.g.*, *Orito et al.*, 2000; *Maeno et al.*, 2001; *Adriani et al.*, 2010].

Computed antiproton differential intensities are shown as functions of kinetic energy, together

with spacecraft observations, in Fig. 5.11. Note that the red line in the figure denotes results for $qA > 0$ which, given the charge sign of the particles in question, is applicable to the $A < 0$ magnetic polarity cycle. Hence intensities computed with the 3D modulation code during $A < 0$ are greater than those for $A > 0$, as expected for these negatively charged cosmic-rays. The amount of modulation, given the relatively small separation between the modelled spectra at 1 AU, and the local interstellar spectrum at the 100 AU boundary, is very low. This result is quite similar to that reported by *Langner and Potgieter* [2004]. Furthermore, although the error bars on the observations are quite significant, it is quite encouraging to note that the results yielded by the *ab initio* 3D modulation code agree rather well with spacecraft data. The same can be said of the ratios of the computed antiproton to proton intensities at Earth, shown as functions of kinetic energy in Fig. 5.12.

The fact that exactly the same parameters that were used in the *ab initio* modulation model to fit proton observation, give quite reasonable agreement with antiproton data, is indeed encouraging. The good agreement with the PAMELA observations reported by *Adriani et al.* [2009a] would imply that the *ab initio* approach employed here handles both species in a self-consistent manner, using the same diffusion and drift coefficients.

5.3 Electron and positron modulation

In this section the effects of various dissipation range turbulence quantities on modelled galactic electron intensities will be considered first. As a point of departure, a reference set of these turbulence quantities is assumed. The reference parallel mean free path is chosen to be the random sweeping result described in Sections 4.3 and 4.4, utilizing the *Leamon et al.* [2000] fit through origin proton gyrofrequency model for the dissipation range breakpoint wavenumber (see Subsections 2.3.5 and 4.5.1), and choosing the dissipation range spectral index to be equal to 2.6, after *Smith et al.* [2006]. In what is to follow, the same 2D outerscale as for protons is used, where $\lambda_{out} = 12.5\lambda_{c,2D}$, and a Parker HMF is again employed.

5.3.1 Effect of the dissipation range breakpoint wavenumber

Figure 5.13 shows galactic cosmic-ray electron intensities as functions of kinetic energy at Earth and at 5 AU, for the extrapolated *Leamon et al.* [2000] models for the dissipation range breakpoint wavenumber k_D. There is a clear charge-sign dependence in the solutions, with intensities corresponding to $A < 0$ conditions (hence, $qA > 0$) being consistently larger than those corresponding to $A > 0$ conditions. At the highest energies shown, the choice of k_D has virtually no effect on the computed electron intensities. This is a consequence of the fact that the electron parallel mean free paths employed here are essentially independent of quantities pertaining to the dissipation range on the slab turbulence power spectrum at these energies. The intensities yielded by this approach are in relatively good agreement with the high energy

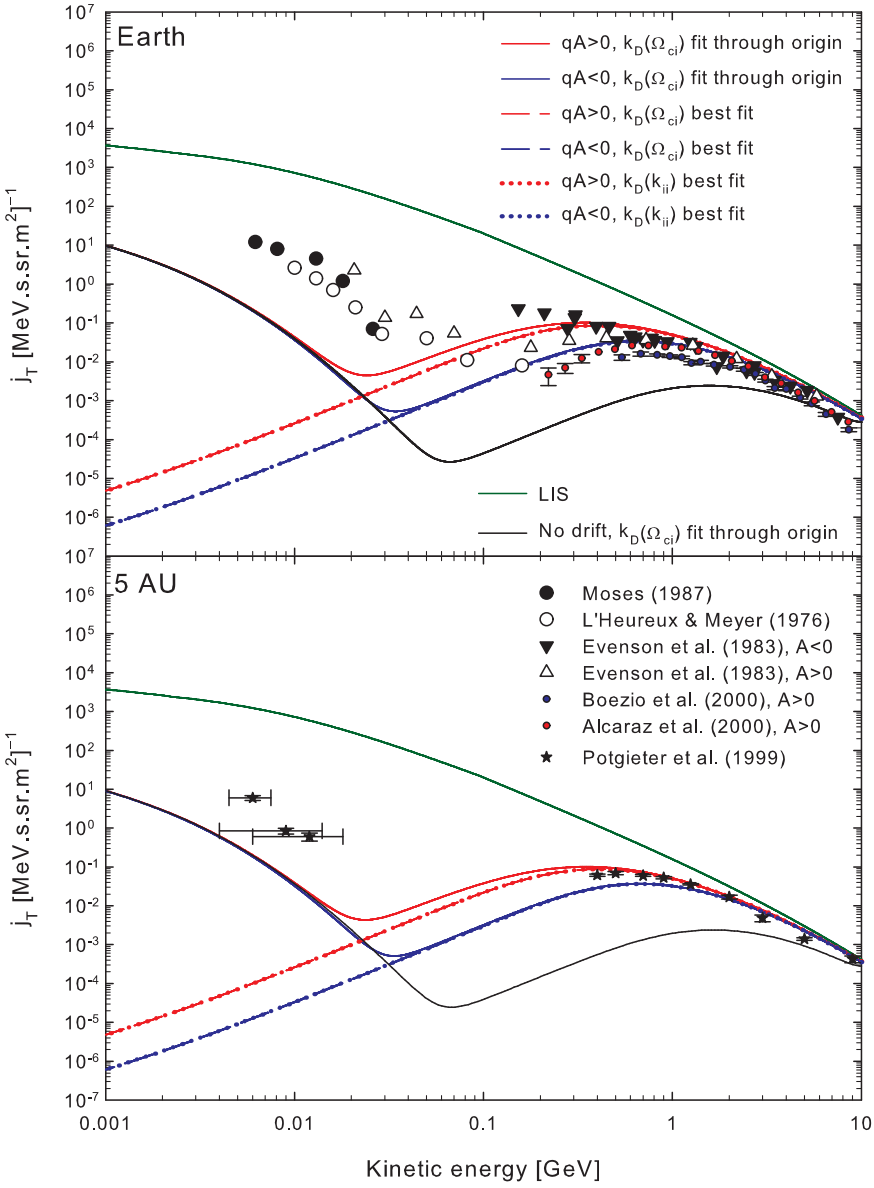

Figure 5.13: Galactic cosmic-ray electron intensity spectra at Earth (top panel) and at 5 AU (bottom panel), as a function of kinetic energy for various *Leamon et al.* [2000] models for the dissipation range spectral breakpoint wavenumber. Spacecraft data shown are reported by *Moses* [1987], *L'Heureux and Meyer* [1976], *Evenson et al.* [1983], *Boezio et al.* [2000], *Alcaraz et al.* [2000] and *Potgieter and Ferreira* [1999].

observations shown, for both magnetic polarity cycles, and at both radial distances considered.

At intermediate to low energies, however, the effects of the different models for the dissipation range breakpoint wavenumber become more readily apparent. Both best-fit models lead to spectra that are essentially identical, and display a strong charge-sign dependence down to the lowest energies shown. Use of the fit through origin proton gyrofrequency model for k_D, however, yields intensities that show a clear increase at intermediate energies, following the trend of the observations but remaining below them, and relax towards the no-drift solu-

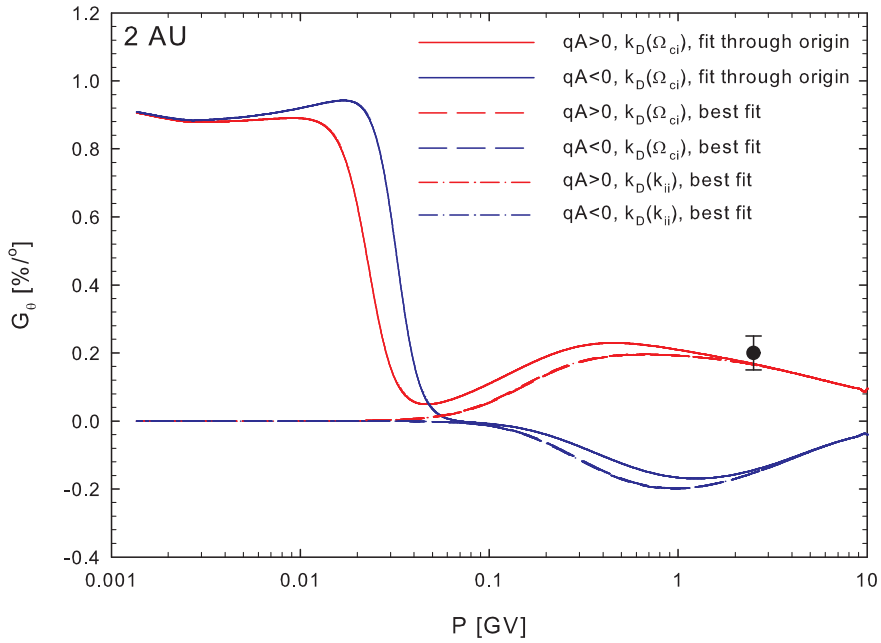

Figure 5.14: Galactic cosmic-ray electron latitude gradients at 2 AU, as a function of rigidity for various *Leamon et al.* [2000] models for the dissipation range spectral breakpoint wavenumber. Spacecraft data point shown is that reported by *Heber et al.* [2008].

tion corresponding to the fit through origin proton gyrofrequency model shown in Fig. 5.13, as expected when drift effects become unimportant at low energies [see, *e.g.*, *Potgieter*, 1996]. Below ~ 0.1 GeV all computed spectra display an E^2 kinetic energy dependence, a hallmark of having relaxed to the relativistic adiabatic limit [*Caballero-Lopez et al.*, 2010]. Spectra computed using the best-fit models for k_D, however, remain in this limit down to the lowest energies shown. These differences in the solutions corresponding to the various models for k_D can be understood in terms of the behaviour of the parallel mean free paths in the the outer heliosphere. From Subsection 4.5.1, and 4.5.2, the fit through origin proton gyrofrequency model yields the smallest values for k_D of the various models in the outer heliosphere, and hence the largest values for the electron parallel mean free path at small rigidities. The best-fit models yield very similar values for k_D in this region, and consequently very similar parallel mean free paths, considerably smaller than those for the fit through origin proton gyrofrequency model. As the ENLGC perpendicular mean free paths here used are functions of $\lambda_{\parallel}$, this reasoning applies equally to their behaviour at lower rigidities, and explains the similarity of the cosmic-ray intensities computed when the best-fit models for k_D are employed. The charge-sign dependence seen at the lowest energies for electron intensities when the best-fit models for the dissipation range breakpoint wavenumber are used is then a direct consequence of the fact that, due to the smaller parallel and perpendicular mean free paths for these models, drift effects dominate the transport of the galactic electrons at low energies, which is clearly not the case when the fit through origin proton gyrofrequency model for k_D is applied.

The computed galactic electron latitude gradients, illustrated in Fig. 5.14, appear independent

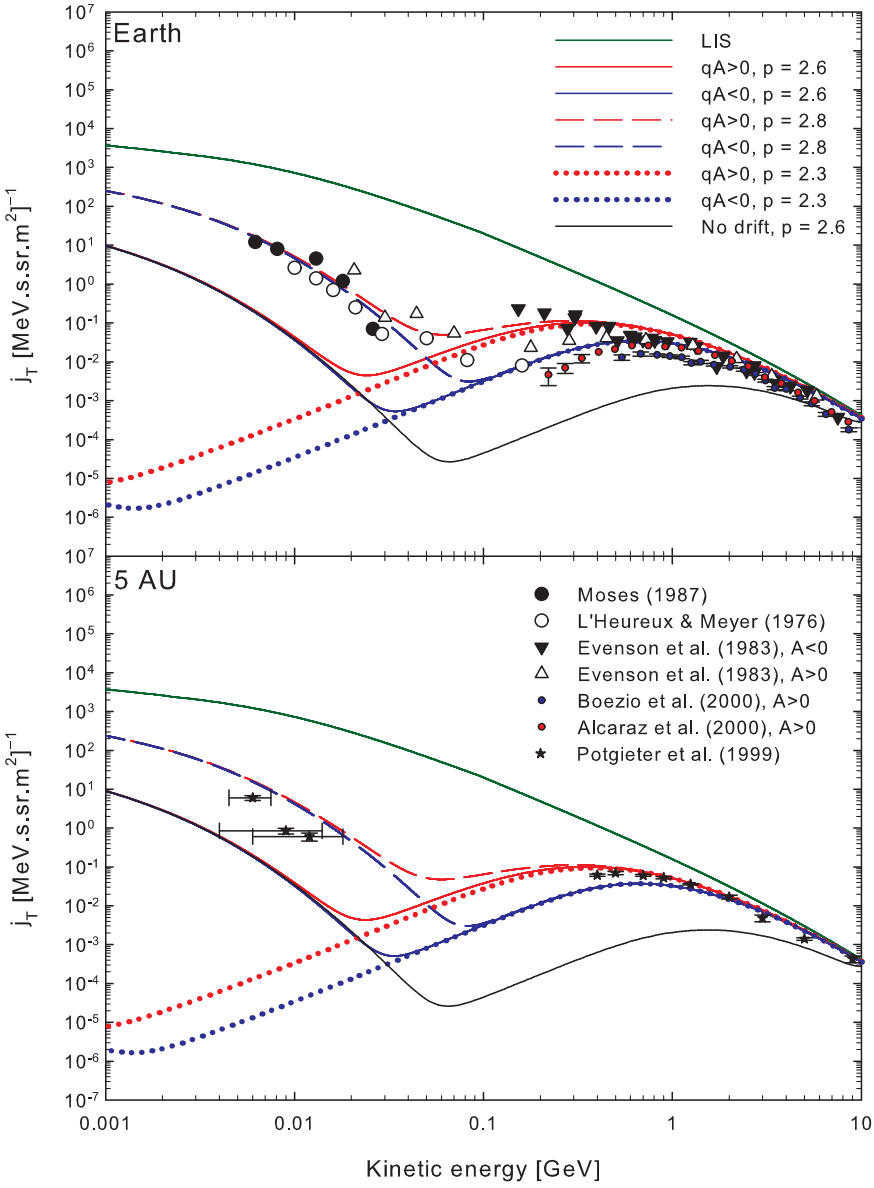

Figure 5.15: Galactic cosmic-ray electron intensity spectra at Earth (top panel) and at 5 AU (bottom panel), as a function of kinetic energy for various values for the dissipation range spectral index. Spacecraft data shown are reported by *Moses* [1987], *L'Heureux and Meyer* [1976], *Evenson et al.* [1983], *Boezio et al.* [2000], *Alcaraz et al.* [2000] and *Potgieter and Ferreira* [1999].

of the dissipation range breakpoint wavenumber at the highest rigidities shown, for the same reason as outlined above. The signs of latitude gradients for $A > 0$ and $A < 0$ are as expected of negatively charged cosmic-rays [see, *e.g.*, *Jokipii and Thomas*, 1981], in that latitude gradients corresponding to $A < 0$ (*i.e.* $qA > 0$) are positive, and *vice versa*. The computed $qA > 0$ latitude gradients shown all agree, within uncertainty, with the *Heber et al.* [2008] data point shown. At lower rigidities, the effects of the various models for k_D can clearly be seen, with the results for the fit through origin proton gyrofrequency model relaxing to the no-drift values at the lowest energies shown. The latitude gradients for the best-fit models for k_D are very similar, again due to the similarity of the mean free paths yielded by these quantities. At intermediate rigidities,

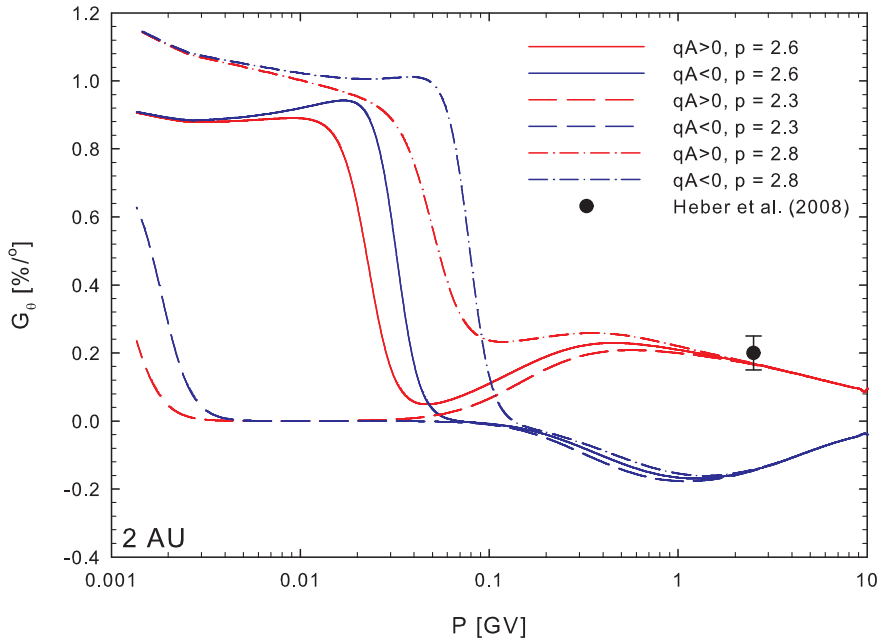

Figure 5.16: Galactic cosmic-ray electron latitude gradients at 2 AU as a function of rigidity for various values for the dissipation range spectral index. Spacecraft data point shown is that reported by *Heber et al.* [2008].

however, use of the best-fit models for k_D leads to somewhat smaller latitude gradients than for the case of the fit through origin proton gyrofrequency model during $qA > 0$, and somewhat larger latitude gradients during $qA < 0$. This is due to the greater effects of drifts, relative to the smaller mean free paths acquired for the best-fit models for k_D. The disappearance of the latitude gradients computed for the best-fit k_D models below about 0.1 GV is a consequence of the adiabatic cooling of these cosmic-rays [*Caballero-Lopez et al.*, 2010], and occurs when the E^2 behaviour is seen in the energy spectra shown in Fig.5.13. At the lowest energy shown, latitude gradients again become finite, and the spectra in Fig.5.13 start to increase from the E^2 limit

5.3.2 Effect of the dissipation range spectral index

The results of the previous subsection show that the use of the fit through origin proton gyrofrequency model yields galactic electron intensities in reasonable agreement with observations at high energies, and qualitative agreement at lower energies. Therefore this model for k_D is chosen as a reference model, with which the effects on cosmic-ray intensities of other quantities that influence the behaviour of the low rigidity electron mean free paths will be compared. This subsection aims to illustrate the effect that varying the dissipation range spectral index, within the range $p = 2.61 \pm 0.96$ reported by *Smith et al.* [2006] at Earth, would have on these intensities.

Galactic electron intensities computed assuming values of 2.3, 2.6 and 2.8 for the dissipation

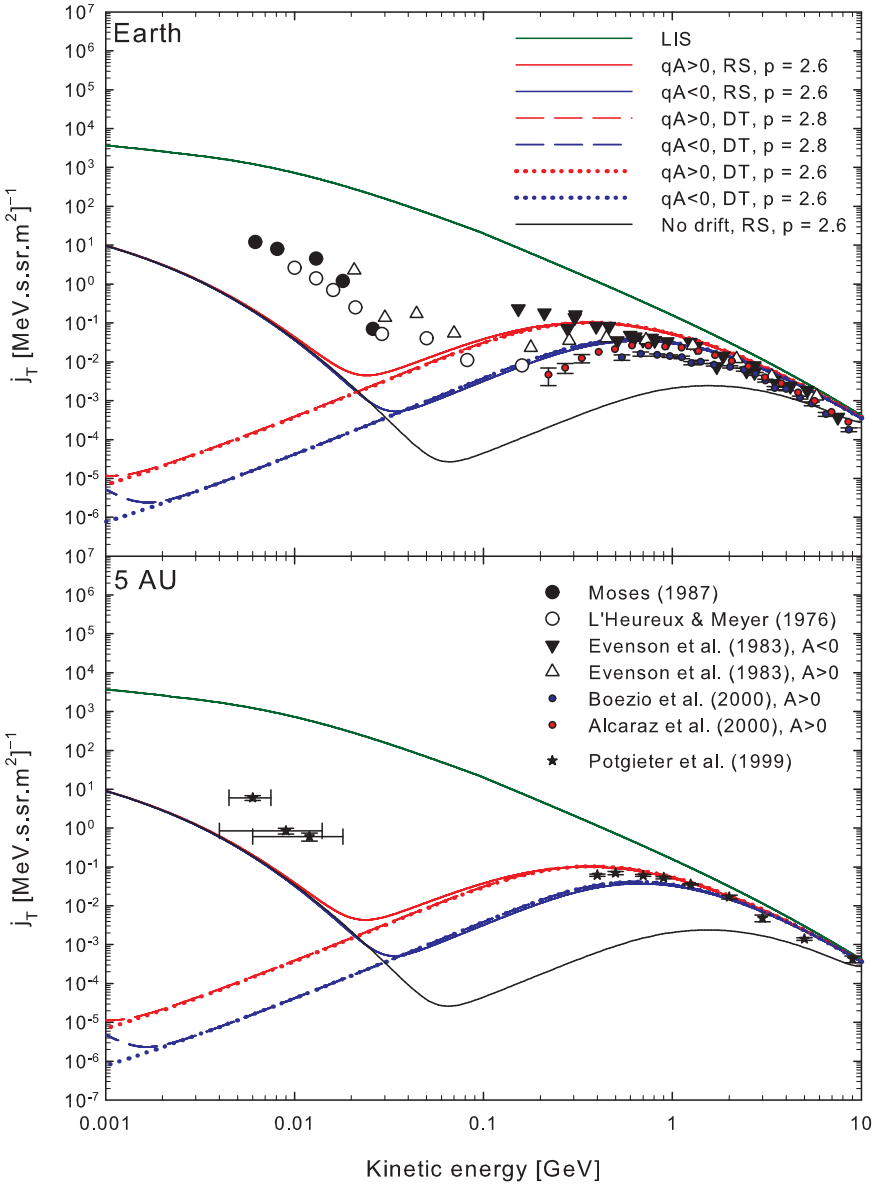

Figure 5.17: Galactic cosmic-ray electron intensity spectra at Earth (top panel) and at 5 AU (bottom panel), as a function of kinetic energy for parallel mean free paths acquired assuming the random sweeping (RS) and damping (DT) models for dynamical turbulence. Spacecraft data shown are reported by *Moses* [1987], *L'Heureux and Meyer* [1976], *Evenson et al.* [1983], *Boezio et al.* [2000], *Alcaraz et al.* [2000] and *Potgieter and Ferreira* [1999].

range spectral index are shown as functions of kinetic energy both at Earth, and at 5 AU in the ecliptic, in Fig. 5.15. From Subsection 4.5.2, an increase in p leads to a larger low-rigidity electron parallel mean free path, which in turn leads to a larger low-rigidity perpendicular mean free path. The effects of this are evident in Fig. 5.15, where the smaller mean free paths implied by $p = 2.3$ lead to a drift dominated electron spectrum at both 1 AU and 5 AU. It is interesting to note that at the very lowest energies, the $p = 2.3$ solutions show the slightest indication of turning up, after displaying the relativistic adiabatic limit E^2 kinetic energy dependence seen in Fig.5.13. The $p = 2.8$ case yields intensities large enough to agree with the low energy *Moses*

[1987], *L'Heureux and Meyer* [1976], and *Potgieter and Ferreira* [1999] spacecraft data. These data are usually assumed to consist largely of Jovian electrons, and can in that light be viewed as an upper limit for the current comparison. *Evenson* [2011], however, argues that due to the differences in the power-law behaviour of low energy electron spectra observed by means of balloon-borne experiments with those expected of Jovian electron intensities, the galactic component at energies below 100 MeV may be the predominant one. Above about 0.1 GeV, as before, the choice of dissipation range spectral index has no effect, due to the nature of the parallel mean free paths here employed.

Figure 5.16 shows computed latitude gradients as functions of rigidity, calculated at 2 AU for the various values here considered for the dissipation range spectral index. At lower rigidities, the $p = 2.8$ and $p = 2.6$ cases relax to the no-drift scenario, with latitude gradients for the larger value of p being significantly larger below about 0.1 GeV. To determine at what energy a no-drift scenario occurs for the $p = 2.3$ case would require runs to lower energies, although the latitude gradients for this case do show an increase at the very lowest rigidities considered. Before this increase, however, latitude gradients for the $p = 2.3$ case vanish, due to the effects of adiabatic cooling [*Caballero-Lopez et al.*, 2010]. At the highest rigidities, varying the dissipation range spectral index has no effect on the latitude gradients, as expected.

5.3.3 Effect of the assumed model for dynamical turbulence

From Section 4.5 it is clear that the choice of the random sweeping or the damping model for dynamical turbulence has a significant effect on the low-rigidity electron parallel mean free paths. The effects this choice has on computed galactic electron intensities will be the subject of this subsection. Here a random sweeping parallel mean free path expression employing the fit through origin proton gyrofrequency model for the dissipation range breakpoint wavenumber, with a value of $p = 2.6$ for the dissipation range spectral index, will be assumed as a reference.

Figure 5.17 shows computed galactic electron intensities at 5 AU and at Earth for the random sweeping and damping turbulence mean free paths where $p = 2.6$, and the damping turbulence parallel mean free path where $p = 2.8$. It is immediately clear that the use of the damping turbulence mean free paths, these being consistently smaller than their random sweeping counterparts, leads to drift dominated electron intensities at lower energies. This is the case even when $p = 2.8$. This latter case, however, does show some increase at the very lowest energies shown. This is an intriguing result, in that the damping turbulence model yielding low-rigidity electron parallel mean free paths at Earth closest to the *Palmer* [1982] consensus range, as opposed to the random sweeping parallel mean free path which yields values considerably above this range, results in computed intensities at Earth which in no way can be construed as realistic. This highlights the potential dangers of drawing conclusions as to diffusion coefficients based on 1 AU data, and extrapolating such conclusions throughout the heliosphere. At higher energies, the choice of model for dynamical turbulence does not affect

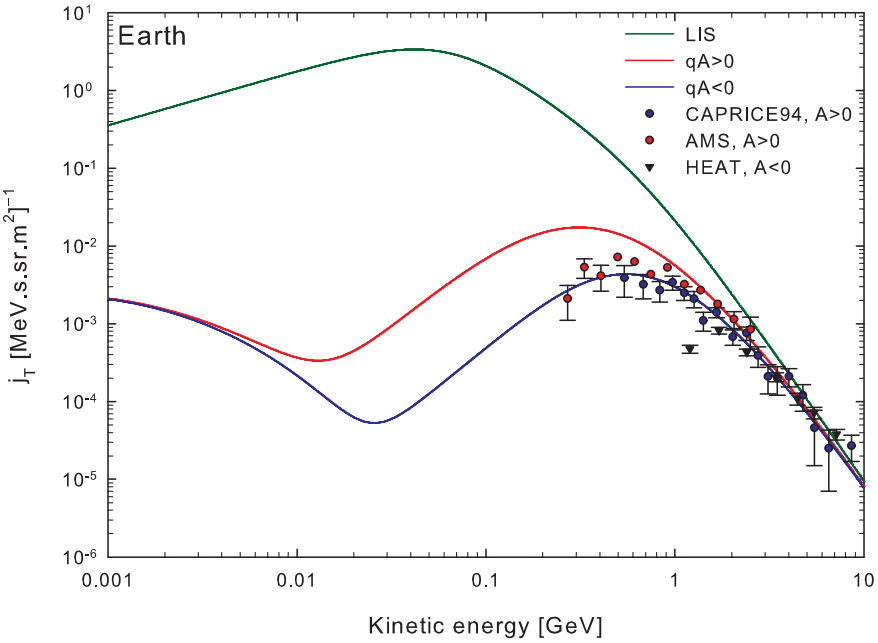

Figure 5.18: Galactic cosmic-ray positron intensity spectra at Earth, as a function of kinetic energy for a 2D outerscale that scales as $\lambda_{out} = 12.5\lambda_{c,2D}$. See text for detail as to other pertinent parameter choices. Spacecraft data shown are reported by *Boezio et al.* [2000] (CAPRICE94), *Alcaraz et al.* [2000] (AMS), and *DuVernois et al.* [2001] (HEAT).

the computed cosmic-ray intensities, as expected from the mean free paths presented in Section 4.5 for the random sweeping and damping turbulence models at these energies, which are essentially identical.

5.3.4 Positrons

As for the case of antiprotons, the question naturally arises as to whether the *ab initio* diffusion tensor here employed in the study of galactic electrons, would fare equally well when the modulation of galactic positrons is considered. Here, the random sweeping electron/positron parallel mean free path described and characterized in Sections 4.3 and 4.5 will be used, assuming the fit through origin proton gyrofrequency model of *Leamon et al.* [2000] for the dissipation range breakpoint wavenumber, and a value of $p = 2.6$ for the dissipation range spectral index. This particular parallel mean free path was chosen as its use led to galactic electron intensities in reasonable agreement with high-energy observations, while also displaying the expected drift-independent behaviour at low energies. The choice of $p = 2.6$ was made due to the fact that, at low energies, the resulting galactic electron intensities remained well below data such as that reported by *Moses* [1987], which is reported to contain a large Jovian electron component.

Computed positron intensity spectra at Earth are shown in Fig. 5.18 as functions of kinetic energy. Solutions corresponding to $A > 0$ conditions remain above those for $A < 0$ at higher

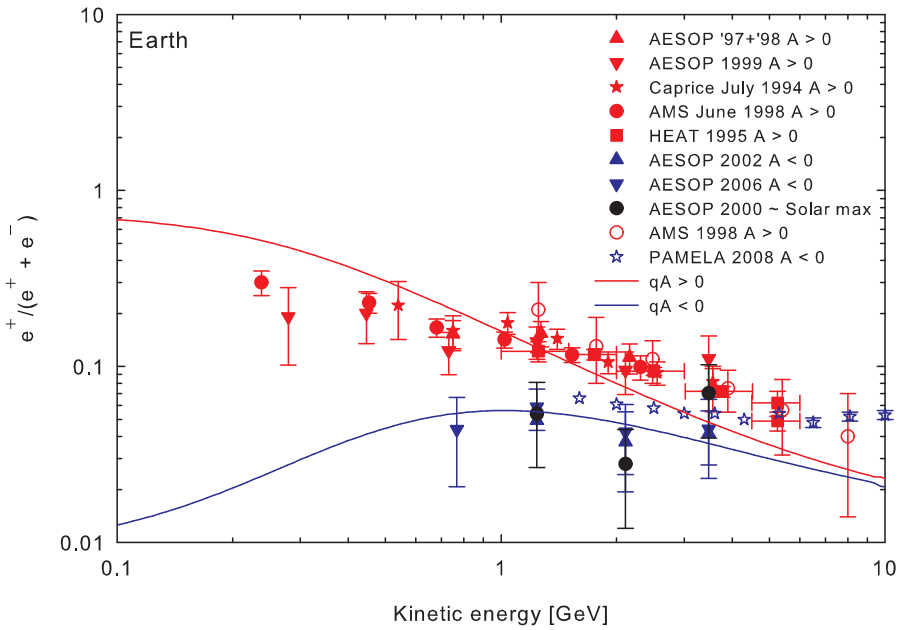

Figure 5.19: Computed galactic cosmic-ray positron ratios at Earth, as a function of kinetic energy for a 2D outerscale that scales as $\lambda_{out} = 12.5\lambda_{c,2D}$, with various observations of this quantity as indicated in the legend. See text for detail as to other parameter choices.

energies, in line with what is expected of the effects of drift on positively charged cosmic-rays [*Jokipii and Thomas*, 1981]. At the very lowest energies, the $A > 0$ and $A < 0$ spectra relax to a no-drift solution, becoming essentially equal, as was the case for galactic electron intensity spectra when the dissipation range parameters here employed were used. Furthermore, at the highest energies illustrated in Fig. 5.18, computed spectra for both magnetic polarities are in good agreement with the observations shown. Below ~ 1 GeV, however, this agreement becomes less good, with computed spectra for $A > 0$ becoming somewhat larger than spacecraft observations at these energies.

As for the case where galactic antiprotons were considered in relation to galactic protons, a comparison of computed positron fractions would provide interesting insights into the efficacy of the current *ab initio* approach in dealing with both electrons and positrons simultaneously. Figure 5.19 shows computed positron ratios for both magnetic polarities as functions of kinetic energy, along with observations of this quantity by various experiments as indicated in the legend. Note that the galactic electron intensity spectra used in the calculation of the positron fraction were acquired assuming the same dissipation range quantities as were employed in the computation of the electron and positron spectra shown in Figures 5.13 and 5.18, respectively.

At the energies shown, the positron fraction during $A > 0$ remains larger than that during $A < 0$. This is to be expected, as electron intensities during $A > 0$ ($qA < 0$) are smaller than during $A < 0$ ($qA > 0$), as shown in Fig. 5.13, the opposite holding true for the positively

charged positrons. Both computed positron fractions remain well below PAMELA observations at the highest energies, as possible primary high-energy positron sources (see *Adriani et al.* [2009b]) are not taken into account in the local interstellar spectrum (Eq. 5.7) employed. Computed positron fractions for $A > 0$ are in reasonably good agreement with the solar minimum observations shown, falling mostly within the range defined by their uncertainties, but also appears to have a steeper energy dependence than the qualitative trend of the data, leading to over-large computed values for this quantity at lower energies. During $A < 0$, the positron fraction computed also agrees reasonably well with the AESOP data, but falls below the lower-energy PAMELA data. This being noted, the *ab initio* approach appears to yield results in fair agreement with observations of positrons, and the positron fraction, for diffusion and drift coefficients exactly the same as those used to compute galactic electron intensities.

5.4 Summary and conclusions

The present chapter aimed to investigate the influence of the *ab initio* diffusion tensor and the two-component turbulence transport model discussed in the previous chapters on the modulation of galactic cosmic-ray protons, electrons, and their respective antiparticles. The 2D outerscale introduced in previous chapters was taken to be a free parameter, in the sense that it is unconstrained by spacecraft observations, and simple, *ad hoc* expressions for it were chosen so as to investigate its effect on computed cosmic-ray spectra. This was done for galactic protons, as the diffusion coefficients for this species are relatively straightforward, and many sets of cosmic-ray data are available for comparisons with model outputs. The 2D outerscale was found to have a significant effect on computed proton intensities, influencing as it does both the perpendicular mean free path and the drift coefficient used. A large outerscale led to results dominated by perpendicular diffusion, while a relatively small outerscale led to drift dominated scenarios. It was found that the form $\lambda_{out} = 12.5_{c,2D}$ gives results that agree reasonably well with cosmic-ray proton energy spectra at Earth, and proton latitude gradients as observed by *Ulysses*.

An interesting result of the *ab initio* approach is the magnitude of computed proton latitude gradients, even when a pure Parker HMF model and axisymmetric perpendicular diffusion were assumed. This led to results that, in some cases, were in good agreement with observations reported for this quantity for $A > 0$ by *Heber et al.* [1996]. Computed latitude gradients for $A < 0$ tended to be too large in absolute value. This issue may in future be resolved by either an alternative spatial dependence for the 2D outerscale, or the use of a novel turbulence-reduced drift coefficient other than the constructed form proposed by *Burger and Visser* [2010] used here.

Agreement of computed with observed galactic proton intensities at larger radial distances was found to be less than good, but this is not surprising given the omission of the effects of the heliosheath in the cosmic-ray modulation code used. That being noted, the forms chosen for the 2D outerscale yielding better agreement between computed and observed proton in-

tensities in the inner heliosphere yielded results considerably larger than observations in the outer heliosphere. This is encouraging, in the sense that qualitatively one would expect this, given the fact that protons observed in the outer heliosphere may have already experienced more modulation than accounted for in the present model. The $\lambda_{2D} = 12.5\lambda_{c,2D}$ form for the 2D outerscale was chosen as a 'best fit' scaling for this quantity and used in all subsequent results considered, leading to reasonable agreement of computed results with observations at high energies for electrons, positrons, and antiprotons.

The effects of a Schwadron-Parker hybrid field as proposed by *Sternal et al.* [2011] were also considered, and found to be very similar to those of the Parker HMF. Computed proton intensity spectra at Earth for both HMF models were found to be essentially the same, with computed latitude gradients only moderately smaller for the hybrid field. This suggests that latitude gradients and intensity spectra, at least as here computed, are more sensitive to the behaviour of the underlying turbulence than to the choice of heliospheric magnetic field model. This is not entirely surprising, as it has been demonstrated in the previous chapter that the spatial variation of the turbulence quantities yielded by the *Oughton et al.* [2011] turbulence transport model has a significant effect on all coefficients of the diffusion tensor. Relative amplitudes of recurring cosmic-ray intensity variations were computed assuming both a reduced Schwadron-Parker hybrid field and a Parker field. The amplitudes computed using the reduced Schwadron-Parker hybrid field were found to be larger than those computed with a Parker HMF. Although qualitatively in agreement with observations, at least in that relative amplitudes for $A > 0$ were found to be larger than those calculated for $A < 0$ at low rigidities, the relative amplitudes yielded by the hybrid field remained considerably smaller than the observations reported by *Zhang* [1997]. Unfortunately, due to issues of stability with the 3D modulation code, the effects of a full Schwadron-Parker field as proposed by *Hitge and Burger* [2010] could not be considered. Only during $A > 0$ does the model yield a relationship between the relative amplitudes and latitude gradients that could be construed as linear, and at least qualitatively in agreement with the findings and explanation presented by *Zhang* [1997]. During $A < 0$, however, it appears that the effects of the wavy current sheet dominate those of the HMF at higher rigidities, since both magnetic field models yield almost identical results for the recurrent intensity variations.

Galactic antiproton modulation was considered next, with the *ab initio* 3D model yielding results in fair agreement with observations of antiproton intensity spectra and of the antiproton/proton ratios at 1 AU. These results were acquired using the same set of diffusion coefficients used for galactic protons.

The computed low-energy galactic electron results presented here displayed an extraordinary sensitivity to various choices of parameters applicable to the dissipation range of the slab turbulence power spectrum. So much so, that even with the omission of a Jovian source, conclusions could be drawn as to which of these parameter's values lead to the most realistic galactic electron intensities. Use of the extrapolated *Leamon et al.* [2000] best-fit ion inertial scale and

proton gyrofrequency models for the dissipation range breakpoint wavenumber yielded very low intensity spectra at low energies with a clear charge-sign dependence, results which are quite unrealistic. Only the use of the fit through origin proton gyrofrequency model for the dissipation range breakpoint wavenumber led to computed spectra in qualitative agreement with observations. Moderate changes in the dissipation range spectral index p, within the uncertainties of the observed value for this quantity reported by *Smith et al.* [2006], yielded results at low energies that were either drift dominated and hence highly unrealistic ($p = 2.3$), or yielded low-energy intensity spectra so high as to be at the level of data reported to have a large Jovian component ($p = 2.8$). Furthermore, the effect of which model of dynamical turbulence has been used in the derivation of the parallel mean free paths can also be seen in the computed low-energy galactic electron spectra. It was demonstrated, for the largest values of p here considered and utilizing the fit through origin proton gyrofrequency model for the dissipation range breakpoint wavenumber, that the damping model of dynamical turbulence yields unrealistic, charge-sign dependent galactic electron spectra at the lowest energies considered. In contrast, the random sweeping model yields mean free paths that lead to a no-drift scenario at low energies.

This sensitivity of the computed low-energy electron spectra to the diffusion coefficients used, raises again the possibility that cosmic-ray electron observations at these energies may be used as a diagnostic from which conclusions as to the behaviour of at least the large-wavenumber component of the slab turbulence power spectrum in the outer reaches of the heliosphere may be drawn. It is also interesting to note that the use of mean free paths derived using the damping model of dynamical turbulence, which at Earth are closest to the *Palmer* [1982] consensus range, leads to unrealistic low-energy electron spectra in the inner heliosphere. This as opposed to the spectra acquired through the use of the random sweeping mean free paths, which remain well above this consensus range at 1 AU. This highlights the potential pitfalls implicit to an extrapolation of diffusion coefficients throughout the heliosphere based on observations at Earth.

At higher energies, dissipation range quantities have no effect on computed galactic electron intensity spectra, which are found to be in relatively good agreement with observations. Computed electron latitude gradients at high rigidities appear to be in good agreement with the admittedly single available data point. At lower rigidities this quantity is clearly very sensitive to parameters pertaining to the dissipation range of the turbulence power spectrum, again raising the possibility that cosmic-ray modulation effects may be useful diagnostics for the behaviour of this part of the slab spectrum. Due to the relative scarcity of latitude gradient observations at low rigidities, however, such an analysis does not appear to be likely in the foreseeable future. Lastly, positron intensity spectra and positron fractions computed with the 'best fit' parameters deduced from electron modulation were compared with observations of these quantities taken at 1 AU, and found to be in reasonable agreement.